Journal of Energy Chemistry 78 (2023) 56–70

Contents lists available at ScienceDirect

Journal of Energy Chemistry

journal homepage: www.elsevier.com/locate/jechem

http://www.journals.elsevier.com/journal-of-energy-chemistry/

Activation of 2D MoS_2 electrodes induced by high-rate lithiation processes

Tianzhu Liu [a], Georgian Melinte [b], Oleksandr Dolotko [a,c], Michael Knapp [a], Beatriz Mendoza-Sánchez [a,*]

[a] Institute for Applied Materials-Energy Storage Systems (IAM-ESS), Karlsruhe Institute of Technology (KIT), Eggenstein-Leopoldshafen D-76344, Germany
[b] Karlsruhe Nano Micro Facility (KNMF), Karlsruhe Institute of Technology (KIT), Eggenstein-Leopoldshafen D-76344, Germany
[c] Helmholtz-Institute Ulm for Electrochemical Energy Storage (HIU), Ulm 89081, Germany

ARTICLE INFO

Article history:
Received 12 June 2022
Revised 31 October 2022
Accepted 7 November 2022
Available online 14 November 2022

Keywords:
2D MoS_2
Liquid-phase exfoliation
Spray-deposition
Conversion processes
Activation mechanisms
Energy storage mechanisms

ABSTRACT

MoS_2 is a highly promising material for application in lithium-ion battery anodes due to its high theoretical capacity and low cost. However, problems with a fast capacity decay over cycling, especially at the first cycles, and poor rate performance have deterred its practical implementation. Herein, electrodes comprised solely of few-layers 2D MoS_2 nanosheets have been manufactured by scalable liquid-phase exfoliation and spray deposition methods. The long-standing controversy questioning the reversibility of conversion processes of MoS_2-based electrodes was addressed. Raman studies revealed that, in 2D MoS_2 electrodes, conversion processes are indeed reversible, where nanostructure played a key role. Cycling of the electrodes at high current rates revealed an intriguing phenomenon consisting of a continuously increasing capacity after ca. 100–200 cycles. This phenomenon was comprehensively addressed by a variety of electrochemical and microscopy methods that revealed underlying physical activation mechanisms that involved a range of profound electrode structural changes. Activation mechanisms delivered a capacitive electrode of a superior rate performance and cycling stability, as compared to the corresponding pristine electrodes, and to MoS_2 electrodes previously reported. Herein, we have devised a methodology to overcome the problem of cycling stability of 2D MoS_2 electrodes. Moreover, activation of electrodes constitutes a methodology that could be applied to enhance the energy storage performance of electrodes based on other 2D nanomaterials, or combinations thereof, strategically combining chemistries to engineer electrodes of superior energy storage properties.

1. Introduction

Over the past decades, lithium-ion batteries (LIBs) have become the main power source for portable electronic devices [1]. They have also found applications in electric vehicles [2] and stationary battery storage systems [3], which demand a higher energy density than offered by current LIBs (150 W h kg^{-1}) [4]. On the other hand, a low power density has been a limitation of the LIB technology as compared to other energy storage technologies such as supercapacitors [5]. The same can be said for long term cycling stability, typically undermined by a series of undesired irreversible secondary reactions [6].

Current commercial LIBs use graphite as anode, which has a limited capacity of 372 mA h g^{-1} [4]. Its poor ion transport properties undermine the power density of LIBs [4]. Moreover, there are standing safety concerns with graphite due to it favouring thermal runaway during cycling [6]. Alternative anode materials include ion-intercalation materials (e.g., other types of carbon and metal oxides), alloy/de-alloy materials such as metals (Sn, Fe) and metalloids (Si, Ge), and conversion materials that include a variety of metal oxides and metal chalcogenides [4].

Transition metal dichalcogenides (TMDs) have attracted attention as promising anode materials [7]. TMDs are compounds with a generalized formula MX_2, where M is a metal atom from groups 4–10, i.e., M = Ti, V, Nb, Mo, W, and X is a chalcogen atom X = S, Se, Te [8]. Each crystal layer of a TMD consists of hexagonally packed M atoms sandwiched in between two layers of X atoms. Intralayer M–X bonds are predominantly covalent, whereas crystal layers are held together by van der Waals forces [8]. Due to its layered structure, TMDs are excellent hosts for ion intercalation. Particularly, MoS_2 has been intensively investigated as anode for LIBs [7]. MoS_2 exists naturally as the 2H polymorph (a unit cell constituted by two layers where atoms have a trigonal prismatic coordi-

* Corresponding author.
E-mail address: beatriz.sanchez@kit.edu (B. Mendoza-Sánchez).

https://doi.org/10.1016/j.jechem.2022.11.007

nation) [9]. The 1 T MoS_2 polymorph (a unit cell constituted by one layer where atoms have an octahedral coordination) is metastable and can be induced by, for example, Li-ion intercalation [9].

2H MoS_2 is active in a 3–0.01 V electrochemical window, where energy storage takes place via ion intercalation and conversion processes delivering a joint theoretical capacity of 669 mA h g^{-1} (Eqs. (1)–(3)) [7]. However, in practice, a higher capacity is realised, e.g., up to 1200–1300 mA h g^{-1} due to the nanoscale structure with high specific surface area [7]. This capacity is 3 times the capacity of graphite. Additional advantages of MoS_2 over other emergent anodes such as Si and Ge include superior performance at higher rates, better cycling stability, and a superior stability to volume expansion [7].

Thanks to its layered nature, MoS_2 can be cleaved into its constituent layers. Numerous synthesis methods have been developed to deliver nanostructured single to few-layers MoS_2 [10]. Particularly, liquid-phase exfoliation (LPE) is a rapid and scalable method that can deliver few-layers 2D nanomaterials, including high quality few-layers 2D MoS_2 [11]. Nanostructured few-layers 2D MoS_2 brings in play additional energy storage mechanisms that take advantage of high surface areas including capacitive and pseudocapacitive processes [12].

On the other hand, spray-deposition is an electrode manufacturing technique that has a tremendous versatility to develop additive-free electrodes of controlled thickness, in the nanometre to the micrometre scale, large areas, in the m^2 scale, and controlled architecture, including a layer-by-layer (LBL) design [13]. Spray-deposition has been used to manufacture electrodes of a variety of nanostructured materials including various 2D nanomaterials [14–17]. LPE and spray-deposition methods are highly compatible and together offer scope for scalability and high throughput of electrode manufacturing methods. Moreover, LBL architectures of 2D nanomaterials enable nanochannels in between 2D nanomaterials that shorten ion transport paths leading to a faster reaction kinetics and, thus, an enhanced power performance [12,18]. Herein, we produced 2D MoS_2 electrodes, consisting of few layers 2H MoS_2 and with a LBL architecture, using a combination of LPE synthesis methods and spray-deposition.

Despite considerable advances in the field, the realisation of the promising potential of 2H MoS_2 as LIB anode is currently hindered by several performance issues, including a poor cycling stability, and a lack of fundamental understanding of energy storage processes. To date, a full picture of the underlying energy storage mechanisms of MoS_2 anodes in the context of LIBs is not yet established. It is generally accepted that ion-intercalation and conversion processes take place during the first discharge (Eqs. (1) and (2)). However, a withstanding debate is whether the conversion process (Eq. (2)) is reversible upon the following charge (Eq. (3)), or, alternatively, oxidation/reduction processes involving Li_2S/S take place (Eqs. (4) and (5)) [7]. The case is further complicated by secondary reactions linked to the formation of a solid electrolyte interface (SEI) occurring at 0.6 V, a potential at which the conversion process also occurs (Eq. (2)) [7]. Moreover, irreversible surface-based processes, such as SEI formation are typically enhanced in nanostructured materials, as compared to their micro-sized counterparts [7].

Herein, energy storage mechanisms of 2D MoS_2 electrodes were investigated using a combination of electrochemical methods and ex-situ Raman spectroscopy. The reversibility of conversion processes (Eq. (3)) was confirmed where nanostructuring was found to play a key role.

Remarkably, 2D MoS_2 electrodes showed an unusual energy storage performance that dynamically evolved over cycling. Capacity vs cycle curves went through a fall-increase-fall-continuous increase trend. The latter continuous rise of capacity over long cycling was an intriguing behaviour that we investigated using a combination of electrochemical and microscopy methods. Our studies revealed that the underlying phenomena are key physical activation processes induced by cycling at high current rates and where the 2D nature of the pristine materials played a key role. Activated electrodes had a superior rate performance and cycling stability than pristine electrodes and other MoS_2-based electrodes previously reported. Activation, thus, is a methodology here devised, to alleviate a long-held problem of cycling stability of ion-intercalation/conversion electrodes.

2. Methods

2.1. Materials

Molybdenum disulphide powder, (MoS_2, 99%, particle size: ~6 μm, Sigma Aldrich), anhydrous N-Methyl-2-pyrrolidone (NMP, >99%, Sigma Aldrich), 2-propanol (IPA, 99%, Sigma Aldrich), branched polyethyleneimine (PEI), (M.W. 70,000, 30% *w*/*v*, aqueous solution, Alfa Aesar), lithium sulphide powder (Li_2S, 99.8%, BASF) and S powder (S, 99.5%, BASF), sodium carboxymethyl cellulose sodium salt (NaCMC, M.W. ~9,000, Sigma Aldrich).

2.2. Equipment

Ultrasonication of suspensions was performed using an ultrasonication bath (Elmasonic P120H, 330 W effective power) and an ultrasonic probe processor (Fisherbrand ultrasonic Q500, 500 W). Suspensions were cooled down using a refrigerated circulation thermostat (CORIO CD-600F, Julabo, USA). Centrifugation was performed using a centrifuge (Thermo Scientific Heraeus Multifuge X1R) equipped with a TX-400 rotor (16.8 cm radius) and a FIBERLite F15-8x 50cy rotor (10.4 cm radius). The concentration of suspensions was determined using a UV–vis-IR spectrometer (Cary 5000, Agilent Technologies). The mass of the electrodes was measured using a microbalance (Sartorius, Germany) with a ±0.01 mg accuracy. Electrochemical measurements were performed in a VMP3 (Bio-Logic, France) potentiostat.

Spray-deposition was carried out using a Flexi-coat spray-deposition coater (Sono-tek Corporation, USA), delivered and installed by Rubröder Group (Germany). It is equipped with two ultrasonic nozzles, two ultrasonic syringes (25 mL, 0.01 to 5.0 mL min^{-1} flow rate range), each integrating an ultrasonic generator (3.5 W power) and an ultrasonic resonating plunger, a Teflon coated hot/vacuum plate (50 cm × 50 cm area, 4 vacuum zones, and capable to reach temperatures up to 150 °C). The ultrasonic nozzles are mounted on a three-axis coordinated motion system using servomotors that can be controlled manually (by a trackball) or by a provided software (PathMaster). Most key functions of the equipment are controlled via the software, including the control of the hot plate (vacuum zones), devices (nozzles, valves, and servomotors), spraying and purging (in manual mode). Equally, spray deposition patterns can be pre-defined, executed and automated using the software.

2.3. Synthesis of 2D MoS_2

Few layers 2D MoS_2 was synthesized by established LPE methods [19–22] with key modifications. Typically, 1.0 g of MoS_2 was processed in 120 mL of anhydrous NMP, placed in a glass jacketed beaker (250 mL) (Scheme 1a and b). Ultrasonication was performed using an ultrasonic probe processor operated at 60% amplitude, using a pulse mode set for 6 s on and 2 s off, for 8 h. During sonication the mix was cooled down by continuously recirculating cold water (18 °C) through the jacketed beaker. The water was recirculated using a refrigerated circulation thermostat. Subse-

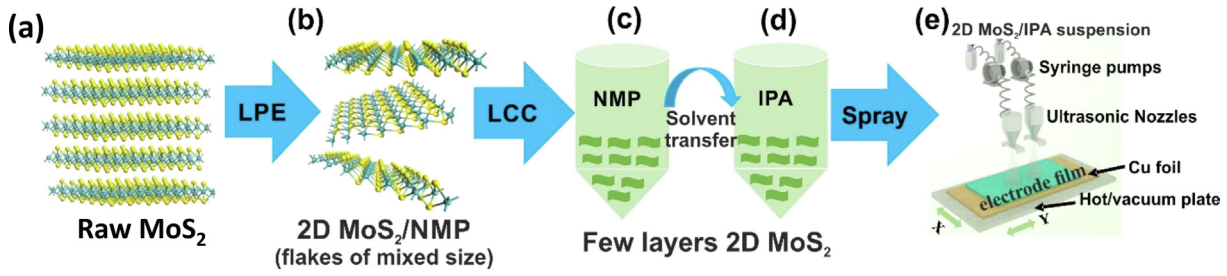

Scheme 1. Synthesis and processing of 2D MoS_2.

quently, a series of centrifugation steps allowed for the separation and selection of few-layers 2H MoS_2 nanosheets, so-called liquid cascade centrifugation (LCC) method (Scheme 1c). The mix was centrifuged first at 2800 r min^{-1} (1475 g) obtaining supernatant 1, which was then centrifuged at 3800 r min^{-1} (2717 g) to obtain the supernatant 2. Subsequently, a solvent exchange of NMP for IPA was carried out using centrifugation—IPA was preferred over NMP due to its lower boiling point and non-toxicity, required for further processing using spray-deposition (Scheme 1d). The final product consisted of few-layers 2D MoS_2 in IPA of typically a 0.1–0.2 mg mL^{-1} concentration. 2D MoS_2/IPA suspensions were then processed by spray-deposition (Scheme 1e).

2.4. Measurement of concentration of suspensions

The concentration of suspensions was determined using UV-vis spectroscopy. The method has been fully described previously [15]. In brief, the active material of a known volume of a suspension of 2D MoS_2 was collected by centrifuge-assistant separation, dried and weighed up. The concentration was then determined. A second volume of the very same suspension was diluted down to prepare aliquots of 0.01 to 0.1 mg mL^{-1} concentration. The absorption of these aliquots was measured using UV-vis spectroscopy in a 200 to 1000 nm wavelength range (Fig. S1a). This included the measurement of the solvent (IPA) as a blank. According to the Beer-Lambert law, $A/l = \alpha C$, where A is absorbance, l is the light path length (1 cm), α is the extinction coefficient and C is the dispersion concentration), a plot of A/l versus C is a line with slope α. Accordingly, A/l values, at a λ = 672 nm, were plotted versus concentration, and a linear fit led to the determination of the extinction coefficient as α = 10.58 cm^2 mg^{-1} (Fig. S1b). The concentration of any suspension was then determined using the Beer-Lambert law and this extinction coefficient.

2.5. Electrode manufacture

2D MoS_2 electrodes were manufactured using a scalable spray deposition method (Scheme 1e). In general, suspensions were syringe-pumped to the ultrasonic nozzles that produced a mist. The mist was deposited onto Cu foil substrates (6 cm × 6 cm area, and thickness of 10 μm), which were set onto a hot/vacuum plate stage heated at 40 °C. The spray deposition process was automatically controlled using a user predefined program. Accordingly, a spray deposition area was defined by 3 coordinates. A spray deposition pattern was developed by continuously spray-depositing material over lines spaced by 2 mm. An aqueous suspension (A) consisted of PEI (0.05 mg mL^{-1}). A suspension (B) consisted of the active material 2H MoS_2 nanosheets/IPA. Suspensions A and B were spray-deposited in a LBL fashion.

Subsequently, the film electrodes were dried in a Buchi-glass drying oven at 70 °C, in vacuum, and cut into 12 mm disks. The average mass load and thickness of the disc electrodes were ~0.3–0.5 mg cm^{-2} and ~3 μm, respectively. The PEI content of the electrode was 1 wt.%.

Electrodes composed of commercially available microsized MoS_2, named in the text raw MoS_2 electrodes, were manufactured following conventional mixing methods. The MoS_2 powder was mixed with carbon black, and NaCMC (binder) in a weight ratio of 8:1:1. The mixture was dispersed in water (500 μL) and stirred overnight. Subsequently, the mixture was coated onto a Cu foil (thickness = 10 μm) using a coating bridge. The electrodes were dried at 80 °C in a vacuum oven for 12 h and cut into 12 mm disks. The average mass loading of the active material and thickness of the disc electrodes were 0.64 mg cm^{-2} and ~15 μm, respectively.

2.6. Materials characterisation techniques

Scanning electron microscopy (SEM) was performed in a Zeiss Supra 55 (Germany). Standard and high-resolution transmission electron microscopy (TEM and HRTEM) were performed using a Themis-Z (FEI, USA). Samples were prepared by dropping suspensions onto standard Holey carbon copper grids.

X-ray diffraction (XRD) was performed on a STOE STADI P diffractometer with Cu $K_{\alpha 1}$ radiation (λ = 1.54060 Å) in transmission mode and at room temperature. Samples were analysed as a powder (raw MoS_2) or as a spray-deposited film (2D MoS_2) onto cellulose acetate and covered up with another such film. A silicon reference (NIST640d) was utilized to account for instrumental contributions and alignment. XRD data were refined using the Fullprof software [23].

Raman spectroscopy was performed on a LabRam Evolution HR800 (Horiba Scientific) using an excitation HeNe-laser (λ = 532 nm). Measurements were carried out using a backscattering geometry. The nominal excitation power at the sample was 39 mW, which was attenuated using a 1% filter. The excitation light was focused and collected using a x100 objective lens, resulting in a spot size of ~5 μm. The scattered light was dispersed using a 600 grooves/mm grating. Samples were measured as powder onto a Si wafer (raw MoS_2) or as dropped flakes onto a glass slide (2D MoS_2/NMP suspension). For measurements of pristine and charged/discharged electrodes, inside a glove box, the electrodes were carefully taken out from coin cells, rinsed with DMC (x3 times) and dried at room temperature for 2 h. Subsequently, the electrodes were sealed in between two pieces of film, Kapton at the bottom (current collector side) and a cellulose acetate film at the top (active material side).

2.7. Electrochemical methods

Two-electrode cells were assembled using either 2D MoS_2 or raw MoS_2 as working electrode and Li foil as counter electrode, both separated by a Celgard 2500 membrane, previously immersed in 70 μL of 1 M $LiPF_6$/ethylene carbonate/dimethyl carbonated (EC/DMC in a 1:1 V/V ratio). Assembly of cells was carried out in an Ar-

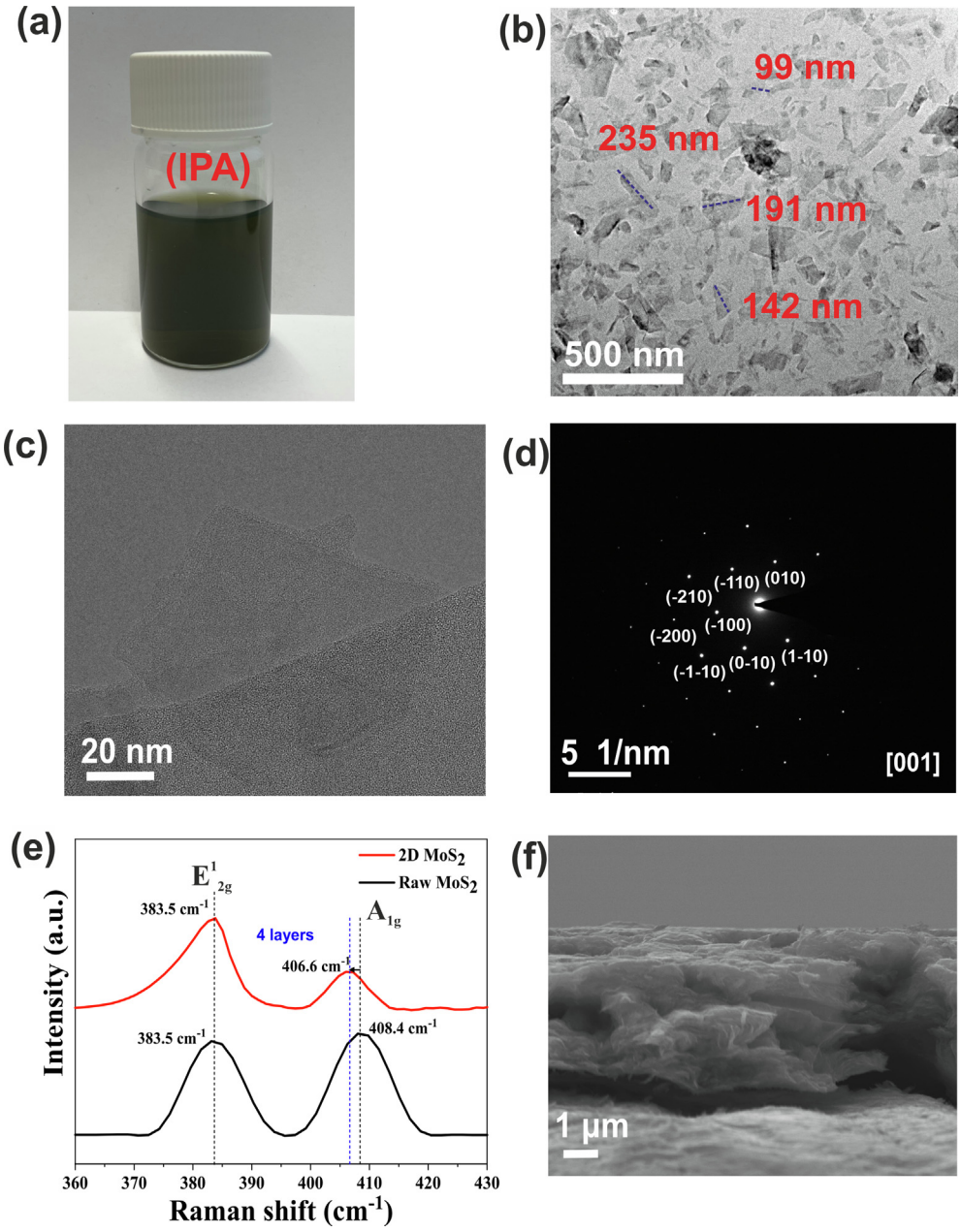

Fig. 1. (a) Optical image of a 2D MoS_2/IPA suspension, (b) TEM image of 2D MoS_2 flakes, (c) HRTEM image of a few-layers 2D MoS_2 flake, (d) SAED pattern of a 2D MoS_2 flake, (e) Raman spectra of raw MoS_2 powder and a 2D MoS_2 flake, (f) SEM image of a cross-section of a spray-deposited 2D MoS_2 film onto a Cu foil. The cross-section shows a LBL arrangement and a thickness of 2.5 μm.

filled glovebox (MBraun, Germany) with oxygen and water concentrations kept both below 0.1 ppm. Electrochemical tests were performed in a temperature-controlled environment at 25 °C.

Cyclic voltammetry (CV) and galvanostatic cycling with potential limitation (GCPL) were performed in a potential range of 3–0.01 V at various scan rates and current densities, respectively. CV for ex situ Raman measurements were performed from OCP down to the desired potential of lithiation or delithiation, the electrode was then left at rest for 3 h. Subsequently, the electrode was taken out from the coin cell and prepared for Raman measurements, as described in the Raman experimental section (above). The CE was calculated as the ratio of charge capacity (ions output) to discharge capacity (ions input) [24].

EIS was performed in three-electrode cells using 2D MoS_2 as working electrode, a Li foil as counter electrode and a Li wire as a reference electrode. Measurements were performed applying an input alternate voltage V_{rms} = 5 mV and in a frequency range from 0.01 Hz to 500 kHz. All cells were discharged to 0.01 V first, then charged to 3.0 V, and then left at rest for 3 h before each EIS measurement. The EIS data was analysed using the Relaxis (rhd Instruments, Germany) software.

3. Results and discussion

2D MoS_2 was synthesized using LPE methods (Scheme 1). (a) Raw MoS_2 is processed by LPE methods to produce (b) 2H MoS_2 flakes, of a range of lateral size and thickness, in NMP suspension; (c) the 2D MoS_2 suspension is purified by LCC methods into few layers 2D MoS_2; (d) few layers 2D MoS_2 in NMP is transferred into

IPA; (e) 2D MoS_2/IPA suspensions are processed by spray-deposition to manufacture electrodes. Suspensions of active material are fed into ultrasonic nozzles via software-controlled ultrasonic pumps. The ultrasonic nozzles, moved in *x* and *y* directions by a software-controlled gantry, produce a mist that is deposited onto Cu substrates. The carrier liquid is evaporated by heat provided by a hot/vacuum plate. Further details of synthesis and processing are given in the experimental section.

The 2D MoS_2/IPA suspensions (Fig. 1a) consisted of flakes of various shapes, e.g., elongated, triangular, and the flake lateral size ranged from 100–200 nm (Fig. 1b). The high structural quality of the 2D MoS_2 flakes, free of defects on the basal planes was confirmed by high-resolution TEM (Fig. 1c). Selected area electrode diffraction (SAED) patterns confirmed a hexagonal crystal structure typical of the 2H MoS_2 phase (Fig. 1d). Bragg peaks, in agreement with the XRD analysis below, could be indexed with the hexagonal phase 2H MoS_2 ($P6_3/mmc$ (No. 194) space group, ICDD 00–002-1133).

The number of layers of the flakes was investigated by Raman. Previous studies have shown that shifts in frequency of characteristic Raman modes of the 2H MoS_2 phase, E^1_{2g} and A_{1g}, are correlated to the number of flake layers [25]. The E^1_{2g} mode, due to in-plane S atom vibrations around Mo atoms in opposite directions, shifts to higher frequencies as the number of layers decreases from bulk to monolayer [25]. The A_{1g} mode, due to out-of-plane vibrations of S atoms in opposite directions, shifts to lower frequencies as the number of flake layers decreases [25]. The resulting Raman shifts are characteristic of a particular number of layers. Raman studies of raw MoS_2 powder showed E^1_{2g} and A_{1g} modes at 383.5 and 408.4 cm^{-1}, respectively (Fig. 1e). Raman studies of various flakes of 2D MoS_2, directly dropped from a NMP suspension onto a glass slide followed by drying, showed Raman shifts of e.g., E^1_{2g} and A_{1g} modes at 383.5 cm^{-1} and 406.6 cm^{-1}, respectively (Fig. 1e). Respect the bulk MoS_2, the latter shifted from 408.4 to 406.6 cm^{-1}, which is the shift corresponding to a 4-layers flake (using a 532 nm laser) [25]. In a similar manner, at least 10 flakes were measured, and the number of layers was determined from 3 to 4.

Spray-deposited electrodes from 2D MoS_2/ IPA suspensions had a LBL architecture and thickness could be tuned from the nanometre to the micrometre scale. Here, a film of 2.5 μm is shown (Fig. 1f). At basal planes, a microporosity and mesoporosity, further discussed below, were developed upon spray deposition (see Fig. 5a). Raw MoS_2 powder, used as the precursor of the 2D MoS_2, consisted of flakes of 1–10 μm size (Fig. S2).

The crystal structure of the raw 2D MoS_2 material and a film of 2D MoS_2 was studied by XRD. Rietveld refinement (RR) analysis identified both samples as having the hexagonal structure of 2H MoS_2 ($P6_3/mmc$ space group (194), ICDD 00–002-1133) (Fig. 2). Their refined structural parameters are shown in Table 1. The RR took into account the preferred orientation of the crystals along the [001] direction of the 2D-like flakes of the raw MoS_2 powder and the spray-deposited 2D MoS_2 film. In addition, a spherical harmonics function (SHF), model 19 corresponding to the Laue class 6/mmm, was used to account for the Lorentzian contribution to reflection broadening due to anisotropic crystal size effects [26]. Further details of the RR are given in the SI.

The only slightly increased cell parameters of the 2D MoS_2 film indicated its unaltered in-plane and out-of-plane crystal structure upon exfoliation. The refinement using the SHF revealed one order of magnitude crystal size decrease upon exfoliation, which was consistent with microscopy studies (Fig. 1b and Fig. S2). X-ray photoelectron spectroscopy (XPS) studies confirmed the 2H phase of MoS_2 (SI, section S16).

Other structural aspects of the 2D MoS_2 film are worth discussing. First, the diffractogram of the 2D MoS_2 film (Fig. 2b) showed considerable diffuse intensities at scattering angles $2\theta < 30°$. This is mainly due to a contribution of the cellulose acetate film where the 2D MoS_2 film was spray-deposited (Fig. S3). However, there is a small contribution of non-Bragg Debye scattering at 2θ angles around the 002 reflection, which is known to be due to several factors including the finite size of crystallites, i.e., only few stacking layers [28], and to a contribution of rotationally disordered unstacked single-layers [29]. In the case of the 2D MoS_2 film, the former condition played a main role due to a successful exfoliation into a few layers of 2D MoS_2. Surely, a disordered stacking of the flakes was induced by spray-deposition, thus, leading to a degree of diffuse scattering. However, the presence of single-layered MoS_2 is not likely as per the presence of reflections 103 and 105 that described a lattice of at least 2 stacked layers.

Second, the broadening of most reflections of the 2D MoS_2 film diffractogram was primarily attributed to the few stacking layers of the successfully exfoliated 2D MoS_2, as described by the Debye-Scherrer equation [28,29]. In addition, preferred orientation along the [001] direction contributed to the broadening of the 002 reflection. This was evidenced by a comparatively increased preferred orientation parameter G1 of 0.36877 (2D MoS_2) > 0.2179 (raw MoS_2). Anisotropic size contributions to reflection broadening were adequately modelled by the SHF and corresponding parameters reflected the plate-like shape of raw and 2D MoS_2. The calculations showed a lateral flake size (basal plane) of 2D MoS_2 one order of magnitude smaller than the flakes of the raw MoS_2. Strain effects also contributed to reflection broadening. This was

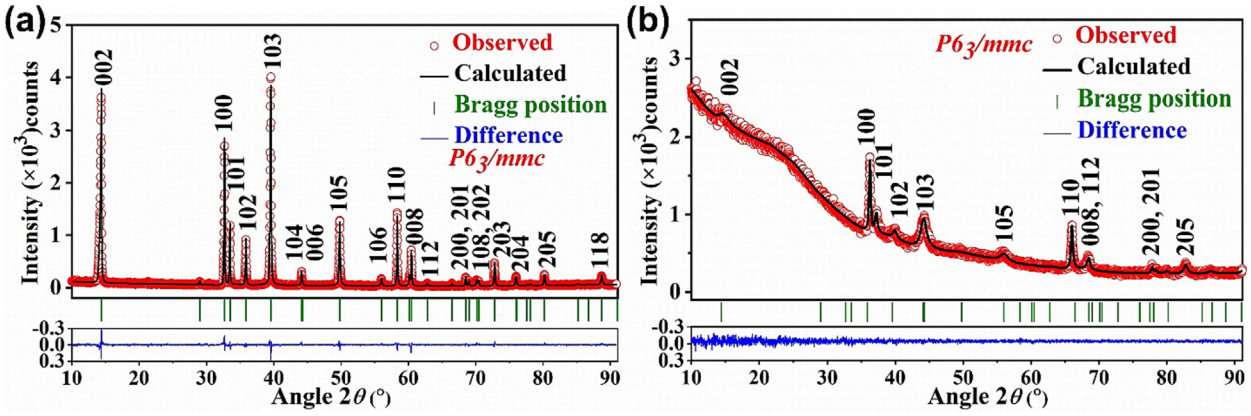

Fig. 2. X-ray diffractograms and corresponding structural model based on RR of (a) raw MoS_2 powder and (b) a spray-deposited 2D MoS_2 film onto an AC film. Vertical bars at the bottom of the chart mark calculated positions of Bragg peaks of the refined phase.

Table 1
Structural parameters of raw MoS_2 powder and 2D MoS_2 film samples determined by Rietveld refinement. The structural data were modelled for Mo atoms occupying the 2*c* (1/3, 2/3, 1/4) position and S atoms occupying the 4*f* (1/3, 2/3, *z*) position. Numbers in brackets give statistical deviations for the last significant digit. Standard deviations have been multiplied by the Berar factor to correct local correlations [27]. Fitting profile (R_p) and weighed profile (R_{wp}) residuals are reported. No correction for background was done.

Sample	Lattice parameters		S atom coordinate z/c	R_p (%)	R_{wp} (%)
	a (Å)	*c* (Å)			
Raw MoS_2	3.1597(2)	12.2962(2)	0.6221(2)	7.4	9.9
2D MoS_2 film	3.1613(2)	12.3126(39)	0.6196(10)	2.1	2.9

evidenced by an increased average strain parameter 12.87% (2D MoS_2) > 6.32% (raw MoS_2).

On the other hand, no asymmetry or a drastic decrease of intensity of reflections was observed, which indicated the absence of translational or rotational defects [28]. Likewise, the 002 reflection showed no 2θ shift with respect to the bulk precursor, which indicated an unaltered interlayer distance [28].

In summary, microscopy studies, XRD, XPS and Raman confirmed the successful exfoliation of bulk MoS_2 into few-layers 2D MoS_2 with and hexagonal 2H crystal structure and high crystal structural quality.

3.1. Electrochemical mechanisms

The lithiation-delithiation mechanisms of MoS_2 have been a focus of interest since the 1980's and since then several points of controversy remain. Two main alternative electrochemical paths have been suggested.

During the first discharge, a lithiation of 2H MoS_2 according to Eq. (1), which occurs at ~1.1 V and involves a phase change from 2H to 1 T polytype as shown in Eq. (1) [30–33]. Then, a conversion reaction has been proposed to occur at ~0.4–0.6 V (Eq. (2)) [34,35], which is accompanied by electrolyte decomposition. Subsequently, upon full charge, Route 1 proposes the reversible oxidation back to MoS_2 (Eq. (3)). It has also been proposed that a de-lithiation of non-reacted Li_xMoS_2 also occurs at ~1.7 V (Eq. (3b)).

The alternative Route 2 proposes lithiation (Eq. (1)), followed by the irreversible conversion (Eq. (2)) during discharge, then followed by oxidation of Li_2S to sulphur S_8, similar to processes occurring in sulphur batteries (Eq. (4)) [7,36]. During a second cycle, sulphur is then reduced to Li_2S (Eq. (5)).

Route 1.

Reduction

$$2H\ MoS_2 + xLi^+ + xe^- \rightarrow 1T\ Li_xMoS_2\ (0 < x < 1,\ \sim 1.1\ V) \quad (1)$$

$$1T\ Li_xMoS_2 + (4-x)Li^+ + (4-x)e^- \rightarrow Mo + 2Li_2S\ (\sim 0.4 - 0.6\ V) \quad (2)$$

Oxidation

$$Mo + 2Li_2S \rightarrow 1T\ Li_xMoS_2 + (4-x)Li^+ + (4-x)e^- \quad (3a)$$

$$1T\ Li_xMoS_2 \rightarrow 2H\ MoS_2 + xLi^+ + xe^-\ (\sim 1.7\ V) \quad (3b)$$

$$Mo + 2Li_2S \rightarrow 2H\ MoS_2 + 4Li^+ + 4e^-\ (\sim 2.4\ V) \quad (3)$$

Route 2.

Eqs. (1) and (2) followed by.

Oxidation

$$Li_2S \rightarrow S + 2Li^+ + 2e^-\ (\sim 2.4\ V) \quad (4)$$

Reduction (second cycle)

$$S + 2Li^+ + 2e^- \rightarrow Li_2S\ (\sim 2.0 - 2.2\ V) \quad (5)$$

Here, energy storage mechanisms of the exfoliated 2D MoS_2 were investigated using electrochemical methods and ex-situ Raman. CVs were performed in a 3–0.01 V electrochemical window at a scan rate of 0.01 mV s^{-1}. During the first cycle, typical cathodic and anodic peaks previously reported in the literature were found (Fig. 3a).

Then, various electrodes were polarized running CVs from open circuit potential (OCP) down to key selected potentials (blue dots in Fig. 3a): 0.74 V and 0.01 V during the first discharge (lithiation), and at 1.98 V and 3.0 V during the first charge (de-lithiation) after the first discharge. The pristine 2D MoS_2 electrode films (Fig. 3b, panel A) showed the typical A_{1g} (out-plane vibration) and E^1_{2g} (in-plane vibration) Raman modes of 2H MoS_2 at 408.6 and 383.6 cm^{-1}, respectively [37,38]. In addition, the Raman mode at 450.7 cm^{-1} has been attributed to a combination of a second order longitudinal acoustic phonon 2LA(M) at the edge of the Brillouin zone and a first order optical phonon A_{2u} (Γ) [25,39]. The broadening observed in this mode is characteristic of nanosized materials due to phonon confinement [39]. The mode at 478.2 cm^{-1} has been discussed in the literature and assigned to a second order quasi-acoustic optical phonon ZA'(B^2_{2g}(M)) [37].

Upon lithiation down to 0.74 V (Fig. 3b, panel B), all the Raman modes of the 2H MoS_2 phase were still present: 475.59 cm^{-1} (ZA'(B^2_{2g}(M))), 455.01 cm^{-1} (2LA(M)), 409.78 cm^{-1} (A^1_g), 384.19 cm^{-1} (E^1_{2g}). In addition, characteristic modes of the 1 T MoS_2 emerged: J_1 at 153.9 cm^{-1}, J_2 at 220.5 cm^{-1} and E^1_g at 288.3 cm^{-1} corresponding to phonons at *M* points of the Brillouin zone, resulting from a Brillouin zone-folding mechanism when a $2a_0 \times a_0$ super lattice of octahedral coordinated and distorted MoS_2 single layers is formed [40,41]. Thus, this confirmed the lithiation process, ongoing at 0.98 V accompanied by a 2H MoS_2 to 1 T Li_xMoS_2 phase transition (Eq. (1)). However, this process was partial as a full conversion of the 2H to the 1 T phase would have implied the absence of the E^1_{2g} mode [40–42]. This lithiation cathodic peak was comparatively broader and of a lower current in the raw MoS_2 electrode (Fig. S5a), which indicated a more efficient lithiation in the nanosized 2D MoS_2 electrode.

Upon further discharge at 0.01 V (Fig. 3b, panel C), two Raman modes at 476.1 and 371.7 cm^{-1} were present. A reference Li_2S (Fig. 3b, panel D), with Raman modes at 477.0 and 371.7 cm^{-1}, confirmed that these modes corresponded to Li_2S. Therefore, this confirmed the occurrence of the conversion reaction at 0.36 V (Eq. (2)). In addition, J_1 at 156.3 cm^{-1}, J_2 at 211.8 cm^{-1} and E^1_g at 281.1 cm^{-1} characteristic of the 1 T MoS_2 phase were still present, which indicated a partial conversion reaction and the prevalence of unreacted 1 T Li_xMoS_2.

Upon subsequent charge (after the first discharge) at 1.98 V (Fig. 3c, panel B), the ZA'(B^2_{2g}(M)) and A_{1g} modes of the 2H MoS_2 phase reappeared at 474.2 and 404.1 cm^{-1}, respectively. A broad band at ~372.2 cm^{-1} was attributed to Li_2S mainly (with a corresponding contribution at the band at 474.2 cm^{-1}), although it might involve a contribution from the E^1_{2g} mode of the 2H MoS_2 phase at 384.2 cm^{-1}. Then, a significant structural change of the 1 T Li_xMoS_2 took place as the modes J_2 and E^1_g modes disappeared, J_1 was present at 156.1 cm^{-1} and new ones emerged at 308.5 and 249.0 cm^{-1}. The latter mode has been theoretically calculated (at 248 cm^{-1}) and corresponds to the frequency of a phonon at the *K* point of the Brillouin

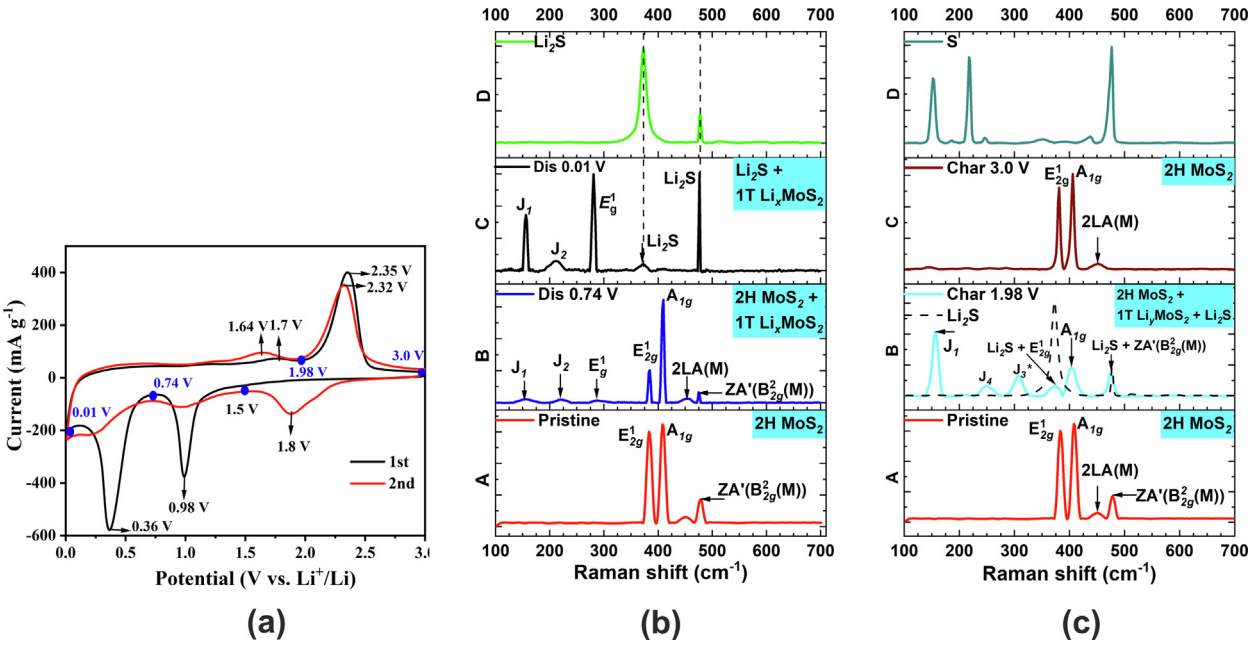

Fig. 3. (a) CVs of a 2D MoS_2 electrode at a scan rate of 0.1 mV s^{-1}. Potentials of current peaks are indicated in black font. Points of polarisation are marked with a blue dot and/or blue font. Ex-situ Raman spectra at various potentials of polarisation upon (b) discharge, and (c) charge of the first cycle. The spectra of the pristine electrode (without polarisation) are shown in panels A for reference. In the same manner, Li_2S powder (panel D in (b)) and sulphur powder (panel (D) in (c)) were used as references.

zone that becomes active as a result of the same zone-folding mechanism that gives origin to J_1 to J_3 modes of the 1 T MoS_2 phase (J_4 in Fig. 3c, panel B) [40]. The former could be a displaced J_3 Raman mode (J_3^* in Fig. 3c, panel B). The reason for this displacement could be linked to significant structural changes of the 1 T MoS_2 phase.

We can conclude that at the shoulder at 1.98 V, unreacted 1 T Li_xMoS_2 was delithiated to produce 2H MoS_2 (Eq. (3b)). A fraction of the 1 T Li_xMoS_2 underwent only a partial delithiation, thus resulting a partially delithiated phase 1 T Li_yMoS_2, where $y < x$, which was structurally very different to 1 T Li_xMoS_2. Hence, the very different Raman modes of such phase at 1.98 V were observed as compared to the phase present at 0.74 V. At this low potential, it was unlikely that the conversion reaction (Eq. (3a)) took place, thus Li_2S was still present in the electrode. In summary, these parallel electrochemical processes led to a mix of 2H MoS_2 + 1 T Li_yMoS_2 + Li_2S in the electrode. Notice that this current peak at 1.98 V was absent in the raw MoS_2 electrode (Fig. S5a), which indicated that early delithiation processes are favoured in nanosized MoS_2 electrodes.

Upon further charging at 3.0 V (Fig. 3c, panel C), Raman modes of the 2H MoS_2 phase were dominant: 451.2 cm^{-1} (2LA(M)), 405.7 cm^{-1} (A_{1g}), 380.9 cm^{-1} (E^1_{2g}). Characteristic modes of the 1 T MoS_2 lithiated phase were still present in a very minor fraction. No Raman modes of sulphur, also studied as reference (Fig. 3c, panel D), were detected. Since Li_2S is not present either, it is concluded that the conversion back to 2H MoS_2 (Eq. (3a)) occurred. In summary, at 2.35 V, conversion (Eq. (3a)) and a nearly full de-lithiation of 1 T Li_x-MoS_2/1T Li_yMoS_2 (Eq. (3b)) confirmed the reversibility of energy storage processes.

During the second cycle, the cathodic current peaks at 0.98 and 0.36 V decreased drastically and a new one arose at 1.8 V; the anodic shoulder at 1.64 V shifted to 1.7 V; and the anodic peak at 2.35 V shifted to 2.32 V (Fig. 3a). The electrochemical activity was also investigated by ex-situ Raman. Electrodes were polarized at 1.5 and 0.01 V during discharge and at 1.98 and 3.0 V in subsequent charge process (Fig. S4). During discharge, at 1.5 V (Fig. S4b, panel B), Raman modes of the 2H MoS_2 and 1 T Li_xMoS_2 were present, which indicated a partial lithiation process (1). Upon discharge down to 0.01 V (Fig. S4b, panel C), only Raman modes of Li_2S were found, indicating a full conversion process (Eq. (2)). Upon charge up to 1.98 V (Fig. S4c, panel B), Raman modes of the 1 T Li_x-MoS_2 and the 2H MoS_2 phase were present, which indicated the occurrence of the conversion (Eq. (3a)) and delithiation process (Eq. (3b)). Upon full charge to 3.0 V (Fig. S4c, panel C), Raman modes of the 2H MoS_2 phase were present, indicating a full conversion process (Eq. (3)).

In summary, Raman studies proved that intercalation and conversion energy storage processes are reversible in the 2D MoS_2 electrode. At intermediate potentials, mixed phases were found describing a partial completion of conversion processes. At full charged and discharged states, full completion of conversion processes was achieved, especially during the second cycle. The capacity loss from cycle 1 to cycle 2, can be attributed to irreversible reactions related to SEI formation and the formation of a "polymeric-like" film, as addressed in the next section.

The role of the nanostructure in the efficiency of energy storage mechanisms was evidenced by the contrast of CVs of the 2D MoS_2 electrodes vs the raw MoS_2 electrodes (Fig. 3a, Fig. S4a). Supporting our views, previous reports on MoS_2 nanosheets have attributed an enhanced efficiency of the reversible conversion process (Eq. (3)) to the large surface area of the nanosheets, where Mo nanoparticles can attach and readily react with Li_2S, while the open structure between nanosheets shortens mass transport paths [43]. In addition, Mo nanoparticles were reported to enhance electrical conductivity paths [43].

In the next sections, the crucial role of electrode morphology and morphology changes undergone over cycling, on energy storage processes were further confirmed.

3.2. Cycling behaviour

Next, the cycling stability and Coulombic efficiency (CE) of 2D MoS_2 and raw MoS_2 electrodes were investigated using GCPL experiments at a current density of 0.05 A g^{-1}.

The discharge capacity decreased from the first to the second cycle in both electrodes (Fig. 4a, Fig. S5b). This was attributed

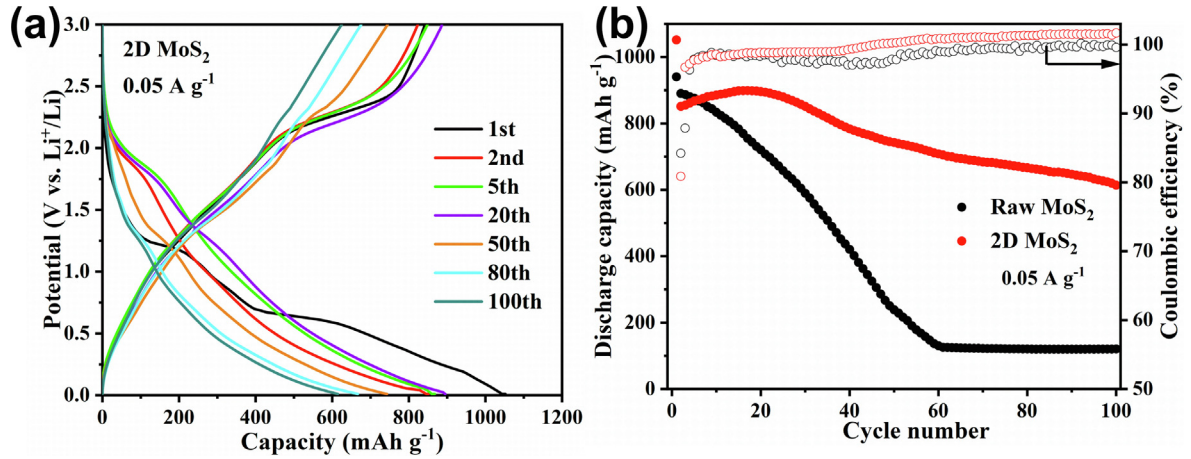

Fig. 4. Electrochemical characterisation of 2D MoS_2 and raw MoS_2 electrodes. (a) GCPL curves of 2D MoS_2 electrode at 0.05 A/g, (b) discharge capacity (solid markers) and Coulombic efficiency (empty markers) vs cycle number curves of 2D MoS_2 and raw MoS_2 electrodes at 0.05 A/g.

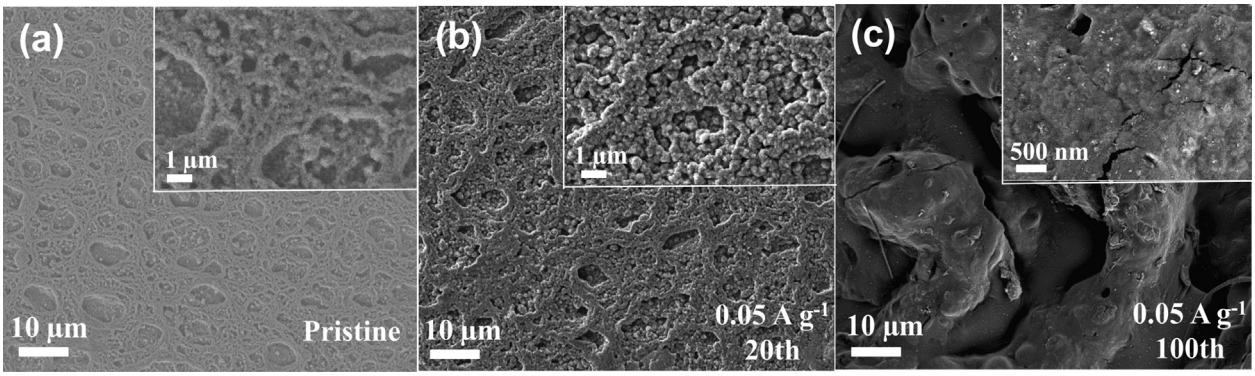

Fig. 5. SEM images of (a) the pristine 2D MoS_2 electrode, and after a GCPL test at a current rate of 0.05 A/g at cycles (b) 20 and (c) 100. Insets show high magnification views of the same image.

mainly to secondary reactions related to the formation of the SEI [44]. However, a second process might have also played a role, especially in the nanostructured 2D MoS_2 electrode. According to previous studies, an additional gel-like film develops on top of the SEI in conversion-type electrodes [45,46]. This film is believed to be composed of organic compounds resulting from electrolyte decomposition at reductive low potentials. The formation of this "polymeric-like" film is thought to be catalysed by metal particles resulting from conversion processes [45,46] as it is the case here with the presence of Mo particles, resulting from the conversion reaction (Eq. (2)). A prior study found that this polymeric-like layer favored pseudocapacitive processes, resulting in an increase in capacity at low potentials [45]. However, as explained by the work, this film inevitably dissolves at high potentials above 2 V [45]. Thus, in the case of 2D MoS_2 electrodes a formation of such a film may have occurred upon discharge contributing to an extra capacity via electrolyte decomposition and pseudocapacitive processes. Upon charge, dissolution of the film prevented a reversible capacity contribution upon the following discharge.

In the subsequent cycles, there were contrasting differences in the cycling behaviour of the 2D MoS_2 vs the raw MoS_2 electrode (Fig. 4a, Fig. S5b). Whereas the raw MoS_2 electrode showed a continuous steep capacity fall, the 2D MoS_2 electrode showed first a capacity increase, from cycles 2–17, followed by a more steadily decreasing capacity (Fig. 4b). At cycles 2–5, the capacity of the raw MoS_2 electrode was higher (890–876 mA h g^{-1}) than the capacity of the 2D MoS_2 electrode (851–867 mA h g^{-1}). In subsequent cycles, the capacity of the 2D MoS_2 electrode was always higher than the capacity of the raw MoS_2 electrode. Morphological studies explained these trends, as described in the next section.

Equally, both electrodes showed a very different evolution of CE upon cycling (Fig. 4b). Initially both electrodes showed a low CE of 84.6% and 77.8% for the raw MoS_2 and the 2D MoS_2 electrodes, respectively. The lower CE of the 2D MoS_2 electrode was attributed to the higher irreversible capacity originated from SEI formation of an electrode of much higher surface area than the microsized raw MoS_2 electrode [44]. Upon charge, and due to the irreversible formation of the SEI, Li-ions experienced a higher diffusion resistance undermining the achieved charge capacity, and, thus, typically causing a decrease of the CE. This effect is enhanced for nanostructured electrodes [44]. Upon further cycling, the CE of the 2D MoS_2 electrode increased rapidly to 98% at cycle 5, reached 100% at cycle 46, and then continuously increased to reach 101.6% at cycle 100. The origin of a small extra charge capacity is not clear at the moment, but most likely it is related to surface-based oxidation processes developed upon cycling. This view is compatible with the occurrence of activation processes, described in the next section. In contrast, the raw MoS_2 electrode reached a value of 98.2% at cycle 5 and remained under 100% during all cycling.

3.3. Morphology

The correlation of the observed cycling behaviour of both electrodes and the electrode morphology was investigated by ex-situ SEM. Spray deposition rendered pristine 2D MoS_2 electrode films where the nanosheets formed ring-like structures of 4–15 μm diameter (Fig. 5a). The size and shape of such structures were determined by the drop size of the spray mist. Inside those ring-like structures, the nanosheets are arranged in a porous structure (inset of Fig. 5a). Nitrogen adsorption isotherms measurements (Fig. S7a) and the application of the Brunauer-Emmett-Teller (BET) method revealed a specific surface area (SSA) of 97.96 $m^2\ g^{-1}$. Barrett-Joyner-Halenda (BJH) pore size analysis (Fig. S7b) confirmed an average pore size of 8.68 nm, confirming a mesoporous structure of the 2D MoS_2 electrodes. In contrast, the raw MoS_2 electrode consists of loosely packed MoS_2 flakes of 1–10 μm size (Fig. S6a), with an SSA of only 35.65 $m^2\ g^{-1}$ and a BJH average pore size of 5.03 nm.

The larger pores and higher SSA of the 2D MoS_2 explain its larger capacity, as compared to the raw MoS_2 electrode, at cycle 1. However, the higher SSA also brought over a larger irreversibility linked to an enhanced SEI formation [44].

During cycles 2–17, the capacity rise of the 2D MoS_2 electrode can be explained in terms of a further opening of its mesoporous structure upon cycling, which facilitates electrolyte infiltration and further exposure of active material to the electrolyte resulting in an enhanced lithiation. In addition, at the nanoscale, opening of nanochannels between 2D nanosheets was likely to occur [18]. Re-stacking of 2D nanomaterials upon removal of solvents during spray-deposition is a well-known phenomenon [15,16]. Cycling, typically, induces the opening of nanochannels, "activating" the electrode for energy storage [12,47]. Activation processes were further investigated by EIS studies (below).

Upon further cycling, up to cycle 100, the 2D MoS_2 electrode showed a compact texture (Fig. 5c), with no evident mechanical degradation. In contrast, in the raw MoS_2 electrode, cracks were evident after 100 cycles (Fig. S6b). This is known to cause full pulverization and failure of microsized electrodes in the long cycling [43]. Thus, the more stable mechanical structure of the 2D MoS_2 electrode allows for a better capacity stability as compared to the microsized raw MoS_2 electrode.

3.4. Cycling at higher rates

The interesting cycling behaviour of the 2D MoS_2 electrodes was investigated further at higher cycling rates. GCPL experiments were performed at 0.5, 1.0, 1.5 and 2.0 A g^{-1} (Fig. 6).

At 0.5 A g^{-1}, the discharge capacity of 2D MoS_2 dropped from 651 (cycle 1) to 562 mA h g^{-1} (cycle 2). Subsequently, the capacity increased up to a peak capacity of 631 mA h g^{-1} at cycle 11. This raising trend is explained in terms of the same activation process described for the experiment at 0.05 A g^{-1}. Subsequently, the maximum of capacity was followed by a fall that reached a minimum of 325 mA h g^{-1} at cycle 85 (Fig. 6a). Remarkably, and unlike the experiment at the cycling rate at 0.05 A g^{-1} (Fig. 4b), this trend was followed by a continuously raising capacity trend until the end of the 500 cycles test (Fig. 6a).

From cycles 1 to 2, the CE increased from 70% to 91% (Fig. 6b). This was expected as per the transition of a highly irreversible regime at cycle 1 to a more stable regime from cycle 2 onwards. During the capacity raising period, at cycles 3–11, the CE stabilized around 94%–95%. During the following capacity drop period, at cycles 12–18, the CE decreased from 93.8% to 90.6%. These reversibility variations can be explained in terms of processes involving the SEI. During the first cycles, it is expected that the SEI first grows steadily enhancing a diffusion control of delithiation

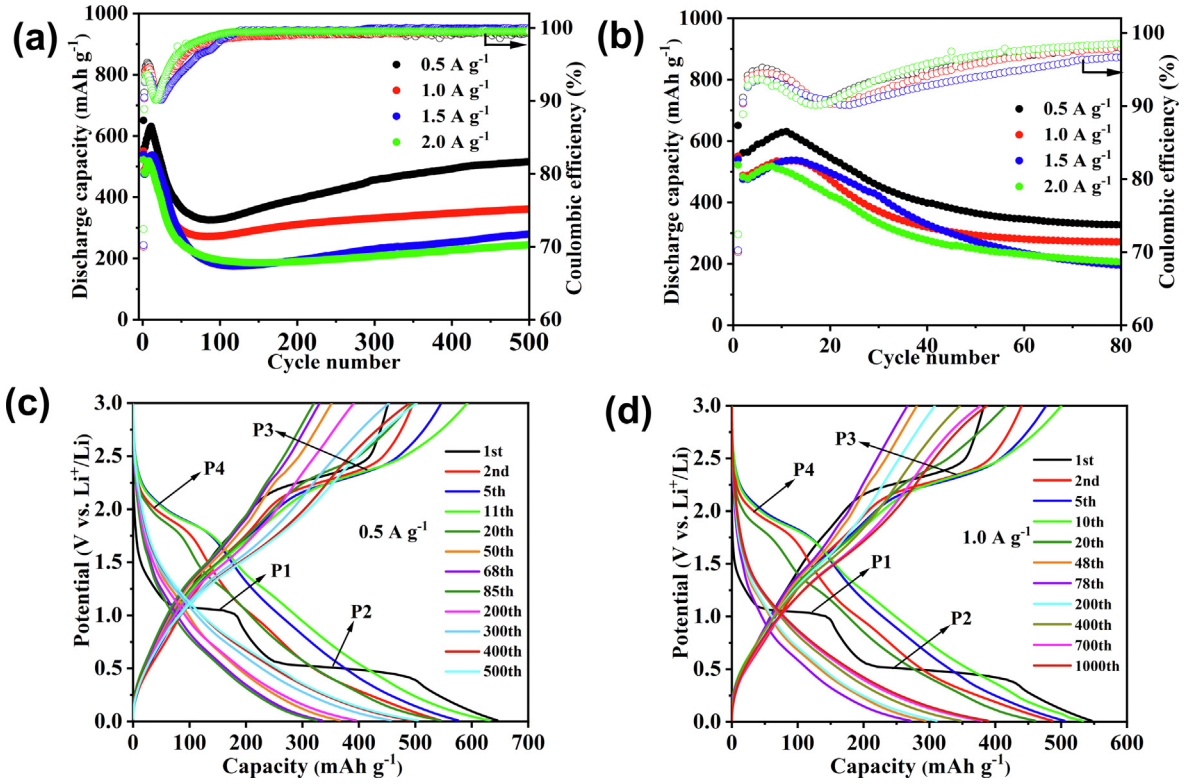

Fig. 6. Electrochemical performance of 2D MoS_2 electrodes. (a) Discharge capacity vs. cycles curves and (b) corresponding insets during the first 80 cycles of 2D MoS_2 electrodes cycled at 0.5, 1.0, 1.5 and 2.0 A g^{-1} current rates and corresponding GCPL curves at (c) 0.5 A g^{-1} and (d) 1.0 A g^{-1} current rates.

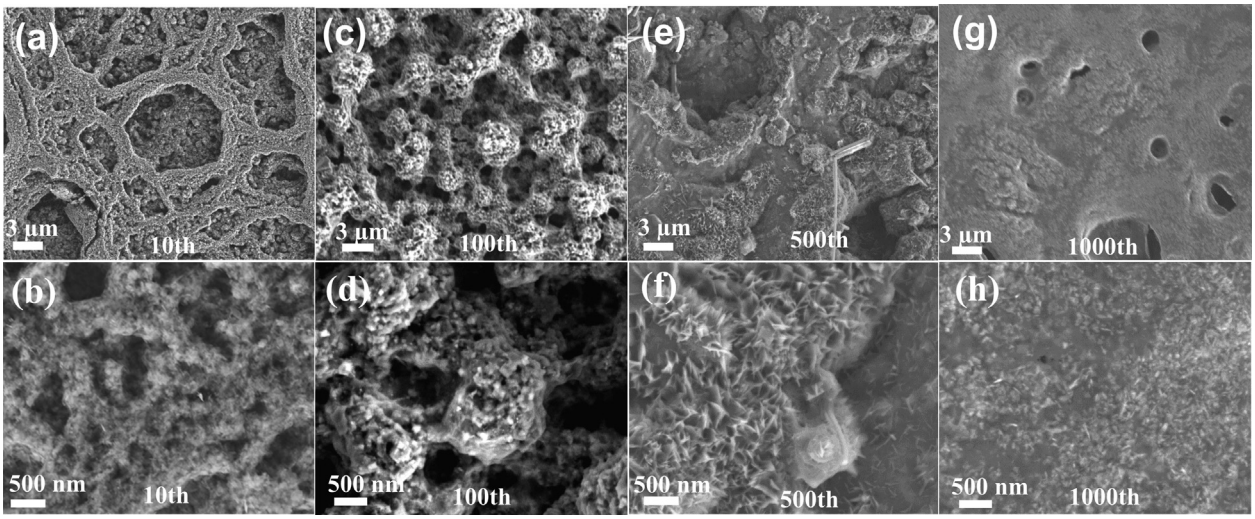

Fig. 7. SEM images of 2D MoS_2 electrodes after GCPL tests at a current rate of 1.0 A g^{-1}. (a,b) at cycle 10, (c,d) at cycle 100, (e,f) at cycle 500, and (g,h) at cycle 1000.

processes [44,48]. After the growing period, the SEI can undergo dynamic changes of formation/decomposition [44,48,49], which was indeed confirmed by EIS studies (below). From cycles 19 until the end of the test, the CE raised, first rapidly up to 98% at cycle 85, describing increasingly reversible processes during the capacity fall stage. Then, from cycles 86 to 500, the CE stabilized at 98%–99%, describing reversible processes during the raising capacity stage.

Analysis of the charge–discharge curves at 0.5 A g^{-1} (Fig. 6c) revealed further information about the ongoing electrochemical processes. The discharge curve at cycle 1 showed the plateau 1, describing lithiation processes at ~1.0 V (Eq. (1)), and the plateau 2 corresponding to the conversion process at ~0.4 V (Eq. (2)). The corresponding charge curve showed a plateau 3, corresponding to the reconversion process at ~2.3 V (Eq. (3)). At the discharge curve 2, the plateaux 1 and 2 vanished and a new and sloppy-one, plateau 4, emerged at ~1.94 V. At the charge curve 2, the plateau 3 at 2.3 V was still present. This curve shape was maintained until cycle 50. Then, featureless curves remained from cycle 50 onwards. In summary, the electrochemical behaviour can be divided into three regimes:

Regime I, dominated by battery processes. At cycle 1–2, battery processes described by Eqs. (1)–(3) were involved.

Regime II, dominated by a combination of battery and pseudocapacitive processes. From cycles 3–50, the sloppy plateaux 3 and 4 vanished progressively, and a sloppy shape was dominant for the rest of the GCPL curves. MoS_2 is known to transition from a battery-type charge storage behaviour to an extrinsic pseudocapacitive behaviour as the particle size decreases from bulk microscale to the nanoscale [50,51]. This is the case for this regime, where battery processes were still in play at plateaux 3 and 4, while pseudocapacitive processes arose due to structural changes induced over cycling (as described below). Indeed, CV studies (below) confirmed that at cycle 3, energy storage processes had a contribution of faradaic and capacitive processes (Fig. 9).

Regime III, dominated by capacitive processes. From cycle 51 until the end of the test, the featureless charge-discharge curves described only capacitive processes with a degree of polarisation, which very likely involved a combination of pseudocapacitive and emerging double layer processes. Morphological changes (as described below) induced an enhancement of surface area that led into enhancement of these capacitive processes.

The following observations can be made.

(1) Since the same type of electrochemical activity, regime II, prevailed during the raising capacity stage 1 (cycles 3–11), it follows that the rise of capacity could not be attributed to a new electrochemical process but rather to physical changes, here proposed as an activation mechanism. The same applies for regime III, where a transition from capacity fall to capacity rise had place. The electrochemical processes before and after this transition were the same.

(2) At cycles 11–18, where the fall of capacity was paralleled by a CE decrease, the same electrochemical processes dominated (regime II). This supports the hypothesis that the observed irreversibility was correlated to physical changes of the electrode and/or changes at the surface of active materials involving SEI formation/decomposition. This view is further supported by the fact that these fluctuating trends of CE at early cycling were observed only at the high current rates of 0.5, 1.0, 1.5 and 2.0 A g^{-1} (Fig. 6b) where surface, rather than bulk, based processes contributed largely to storage but not at the comparatively slower current rate of 0.05 A g^{-1} (Fig. 4b), where bulk processes were more likely to dominate and where the CE increased steadily. EIS studies (below) indeed confirmed a great disruption of the SEI.

(3) The fall of capacity from cycles 12 to 85 involved two regimes, II and III, with not observed change in the falling trend of capacity around cycle 51 (cycle of transition between regimes). This smooth transition indicated that at regime II pseudocapacitive mechanisms dominated increasingly over cycling, while double layer capacitive contributions may have emerged. Nonetheless, a capacity fall trend was kept as a result of a continuous loss of battery processes. However, at cycle 85, the drastic transition to a raising capacity occurred and was dominated by only capacitive processes. We propose that this transition was induced by a second activation process involving further morphological changes of a considerably restructured electrode where surface-based storage processes dominated. This was indeed supported by further microscopy and electrochemical impedance spectroscopy (EIS) studies (see below).

Similar trends in capacity and CE were observed for the tests at 1.0, 1.5 and 2.0 A g^{-1} (Fig. 6a). A similar shape evolution was observed for the charge–discharge curves at 1.0 A g^{-1} (Fig. 6d). At this rate, the cycles of maximum and minimum capacity were cycles 10 and 78, respectively. The capacity, then, increased until cycle 1000. The electrochemical regimes, as defined previously were, regime I (cycles 1 and 2), regime II (cycles 3–48) dominated

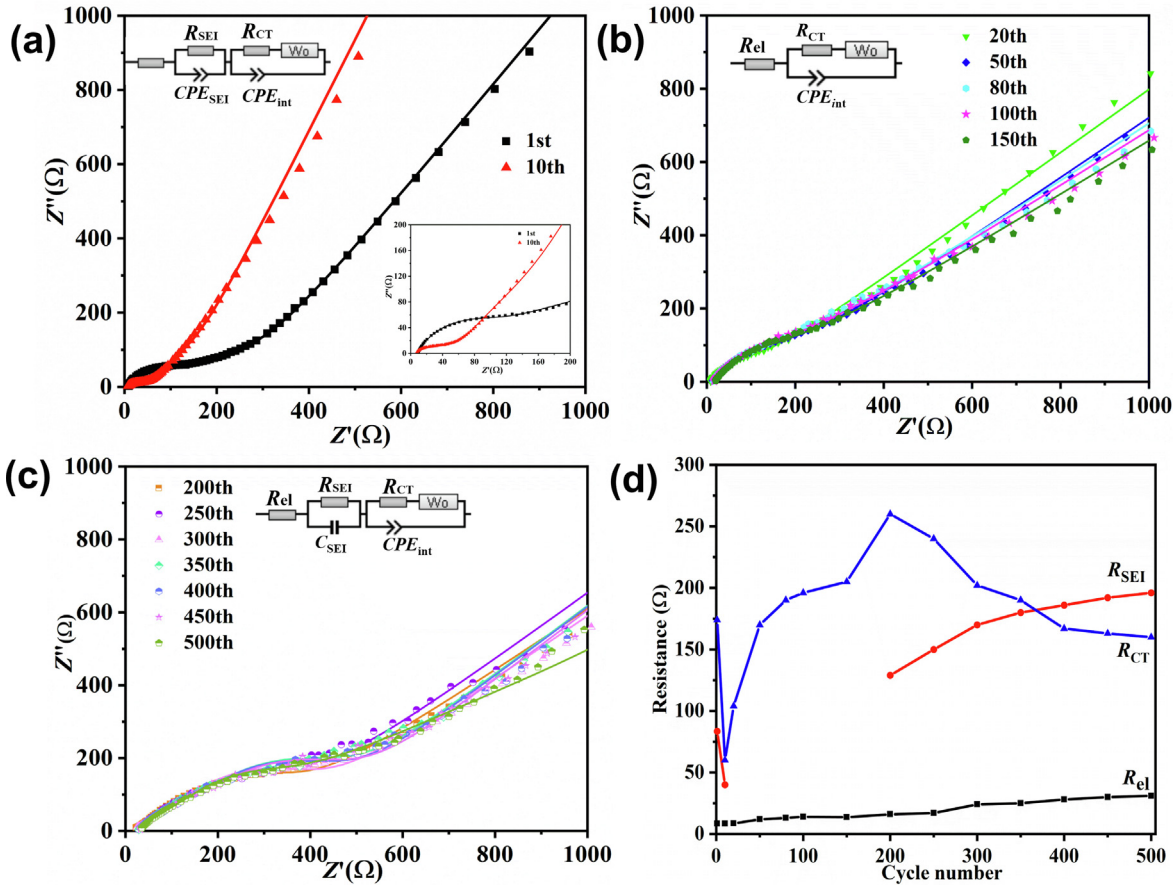

Fig. 8. EIS data (Nyquist plots) of 2D MoS_2 electrodes measured at the end of charge (3.0 V) in a GCPL test at a current rate of 1 A g^{-1} and at cycles: (a) 1 and 10, an inset shows details of data at high frequency, (b) 20 to 150, (c) 200 to 500, (d) corresponding R_{el}, R_{CT} and R_{SEI} vs cycles curves. EECs used for data modelling are depicted in each Nyquist plot.

by a combination of battery and pseudocapacitive process and regime III (cycles 49–1000) dominated by capacitive processes.

3.5. Further microscopy studies

Microscopy studies of the 2D MoS_2 electrode cycled at 1.0 A g^{-1} were performed at the key cycles 10, 100, 500, and 1000 (Fig. 7).

At cycle 10, the end of the initial rise of capacity and within regime II, the electrode showed a nanostructured architecture and an opened mesoporosity (2–50 nm) (Fig. 7a and b) very similar to that of the pristine electrode (Fig. 5a). Therefore, the first activation process at early cycling involved only opening of nanoscale porosity without major microstructural changes. At cycle 100, still around the minimum of capacity at cycle 78 and within regime III, a major microstructural change was observed (Fig. 7c and d); ball-like structures of a diameter of 1–3 μm were formed and organized in a larger porous microstructure with pore sizes ranging from 1–2 μm. Then, during the capacity rise stage, at cycle 500, the architecture of the electrode again changed drastically (Fig. 7e and f). The porosity was closed, the ball-like microsized structures collapsed to form a compact structure comprised of MoS_2 nanosheets that stood vertically. At cycle 1000, the electrode continued to be compact, few pores in the microscale were opened, and the MoS_2 nanosheets were transformed into tiny, needle-like structures (Fig. 7g and h). A very similar restructuration was observed for the electrode cycled at the other current rates. For instance, a very similar compact morphology was found in the 2D MoS_2 electrodes cycled at 0.5 A g^{-1} at cycle 500 (Fig. S8a and b).

It is worth noticing that the raw MoS_2 electrode had a totally different cycling behaviour at 0.5 and 1.0 A g^{-1} (Fig. S9a and b). Unlike the 2D MoS_2 electrodes, the bulk electrodes simply failed as early as 200 cycles and cracks on cycled electrodes were evident (Fig. S10).

EIS studies offered a further insight into energy storage mechanisms.

3.6. Electrochemical impedance spectroscopy

The evolution of the electrical properties at the electrode-electrolyte interface upon cycling was investigated by EIS. The EIS was recorded at key cycles of the long-term cycling tests performed at 0.05 and 1.0 A g^{-1}, and was modelled using various electrical equivalent circuits (EECs) [52,53]:

Model 1: $R_{el}(R_{SEI})(CPE_{SEI})(R_{CT}W_o)(CPE_{int})$.

Model 2: $R_{el}(R_{SEI})(CPE_{SEI})(R_{CT})(CPE_{int})W_o$.

Model 3: R_{el} $(R_{CT}W_o)(CPE_{int})$.

Here, R_{el} is the sum of the resistance of the electrolyte, separator and internal resistance of the cell. A parallel circuit $(R_{SEI})(CPE_{SEI})$ modelled the physics of the SEI where R_{SEI} and CPE_{SEI} are the SEI resistance and capacitance, respectively. The capacitance was modelled using a constant phase element (CPE) accounting for a frequency dispersed capacitance [39,54,55]. A second parallel circuit $(R_{CT}W_o)(CPE_{int})$ modelled the charge storage activity at the electrode–electrolyte interface, where R_{CT} is the charge transfer resistance, CPE_{int} is the capacitance at the interface and W_o is an open circuit terminus Warburg element accounting for diffusion processes [56].

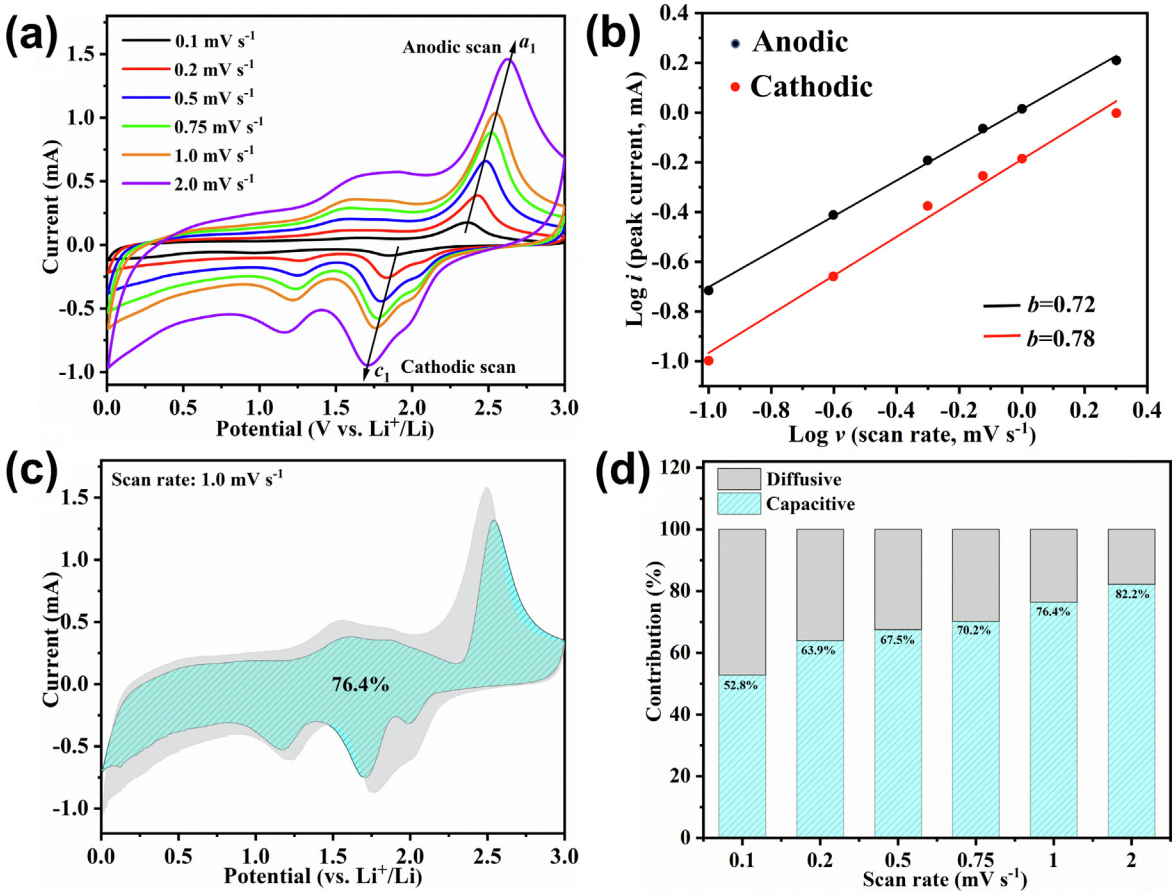

Fig. 9. Evaluation of the kinetic behaviour of 2D MoS_2 electrodes. (a) CVs of cycle 3 at scan rates of 0.1 mV s^{-1} to 2 mV s^{-1}, (b) log (I_i (V_i)) vs log (ν_i) curve at c_1 and a_1 current peaks, (c) CV at 1.0 mV s^{-1} where the capacitive and diffusive contributions to energy storage have been depicted, (d) bar graph describing the percentage contributions to capacitive and diffusion-controlled energy storage at each considered scan rate.

In general, the high frequency data was best fitted to the (R_{SEI})(CPE_{SEI}) circuit, whereas the low frequency data was best fitted to the ($R_{CT}W_o$)(CPE_{int}) circuit. The best model to describe the EIS data at specific cycles is specified, as shown in Fig. 8.

The EIS data of 2D MoS_2 electrodes cycled at 1.0 A g^{-1} was analysed. According to the GCPL experiments (Fig. 6a), key cycles of analysis were chosen: cycle 1, cycle 10 (maximum of capacity), cycles 20–80 in steps of 10 (capacity fall), cycles 100–500 in steps of 100 (capacity rise). The EEC models that apply to the data at different cycles are specified in the text and in Fig. 8.

R_{el} increased from 8.4 Ω (cycle 1) to 31 Ω (cycle 500) (Fig. 8d). This was ascribed to an increase of the cell internal contact resistance upon cycling. Data at cycles 1 and 10 was best described by model 2 (Fig. 8a). From cycles 1 to 10, there was a clear drop of the R_{SEI}, from 83 (cycle 1) to 40 Ω (cycle 10), and the R_{CT} decreased from 174 (cycle 1) to 60 Ω at cycle 10 (Fig. 8d). These impedance properties along with a capacity increase described an activation process where the SEI was thinned and/or broken while mesopores (2–50 nm) and/or micropores (<2 nm) were opened making more efficient the charge transfer at the electrode–electrolyte interface. This was consistent with the morphology of the electrode at cycle 10 (Fig. 7a and b).

As cycling progressed, cycles 20–80, and the capacity fell (Fig. 6b), the EIS data was best described by model 3 involving only the electrode–electrolyte interface (Fig. 8b), which indicates a negligible SEI (Fig. 8d). Meanwhile, the R_{CT} increased drastically from 104 (cycle 20) to 190 Ω (cycle 80). This indicated that the capacity fall stage (Fig. 6b), from cycles 20–80, was underpinned by an electrode restructuration process that destroyed the SEI and increased the electrode–electrolyte interfacial resistance. According to the morphology studies, at this stage, microsized ball-like structures were formed and organized in a microsized porous structure (Fig. 7c and d). In such electrode structure, a good charge transfer is expected at interfaces at pores sites, but not at the centre of the ball-like structures. Thus, an increasing R_{CT} indicated an evolution to larger ball-like structures and smaller pores, without the generation of new micro/nanopores. This, together with a decrease of surface area at the ball-like structures led to a decrease of capacity.

Then, from cycles 80 to 150, the SEI was still negligible and the R_{CT} increased only slightly from 190 Ω (cycle 80) to 196 Ω (cycle 100), to 205 Ω (cycle 150) (Fig. 8b–d). This marked an equilibrium stage, consistent with the minimum of capacity reached during cycling (Fig. 6a). At this stage, the ball-like structures were likely to merge in a more uniform electrode.

Then, from cycle 200 to cycle 500, the R_{SEI} was accountable again, and the EIS data was modelled by a model (see Fig. 8c and d). At this increasing capacity stage (Fig. 6b), the R_{SEI} increased steadily from 129 to 196 Ω, whereas the R_{CT} increased to peak at 260 Ω (cycle 200) to then continuously decrease down to 160 Ω at cycle 500. This describes a second electrode activation (restructuration) process where the SEI is reformed and is steadily growing. On the other hand, cycle 200 marked the end of a process where R_{CT} increased, very likely marking the point of final collapse of the ball-like structures into a more uniform electrode comprised of vertically standing nanosheets, as observed by morphology studies (Fig. 7e and f). This electrode was then of a higher surface

area and had a rich electrolyte infiltration facilitated by structural changes before and after the structure collapse where new micro-/nanopores were likely formed. Rapid ion transport was enabled in this new structure through short nano-channels between vertically aligned tiny nanosheets [57,58]. All these conditions, then, made up for a more efficient charge transfer and the continuous increasing capacity observed.

In comparison, the EIS behaviour of the electrode cycled at a low rate of 0.05 A g^{-1} was very different (Fig. S11a). In this case, the key cycles of the capacity vs cycles curves were cycle 1–2 (capacity fall), 2–17 (capacity rise), then 18–100 (capacity fall). The R_{SEI} was formed at cycle 1, but was negligible until cycle 30, where it was 30 Ω, and continued to increase until cycle 40 (Fig. S11b). The R_{CT} on the other hand, fell from cycle 1 (30.8 Ω) to cycle 10 (20.7 Ω) and then continuously increased until cycle 40 (Fig. S11b). Here, the rising capacity originated from a better charge transfer resulting from the opening of meso/microporosity. Meanwhile the SEI formed at cycle 1 was very thin and unstable. In the falling capacity stage, the SEI formed again at cycle 30 and continued growing. Meanwhile, the R_{CT} of the electrode increased describing a transformation to a compact non porous electrode (Fig. 5c).

3.7. Further investigation of the nature of energy storage processes in place

The nature of the charge storage of the 2D MoS_2 electrodes was investigated by evaluating their kinetics behaviour. Established methods state the dependence of CV current on scan rate as $I_i(V_i) = k_i v_j^b$ (Eq. (6)), where I_i (V_i) is the current at a defined potential $Vi_1,\ldots,Vi_n$, k_i is a constant, v_j is the scan rate considered in a range $j_1,\ldots,j_n$, and b is a constant that defines, the nature of the energy storage in place, i.e., b = 1 describes capacitive processes and b = 0.5 describes diffusion-controlled processes [51,59].

CVs of 2D MoS_2 electrodes were performed at a scan rate range from 0.1 to 2.0 mV s^{-1} (Fig. 9a). CVs were analysed at cycle 3, corresponding to regime II, established by the GCPL studies, where a contribution of pseudocapacitive processes was found. Here, this view was confirmed and quantified. The CVs showed cathodic peaks at c_1 = 1.88 V and c_2 = 1.04 V, and anodic peaks a_1 = 2.31 V and a_2 = 1.64 V (Fig. 9a). The evolution of the current with scan rates was evaluated for the main anodic and cathodic peak (c_1, a_1). The obtained b values were b = 0.72 for c_1 and b = 0.78 for a_1, describing a mix of faradaic and capacitive processes at these particular potentials.

The contributions of each individual process to energy storage over the entire CV were calculated according to $I_i(V_i) = k_{1i}v_j + k_{2i}v_j^{1/2}$ (Eq. (7)), where variables are defined as in Eq. (6) and the first and second terms account for the capacitive and diffusion-controlled processes, respectively [51,60]. A rearrangement of Eq. (7) as $I_i(V_i)/v_j^{1/2} = k_{1i}v_j^{1/2} + k_{2i}$ (Eq. (8)) allows to calculate k_1 and k_2 when plotting $I_i(V_i)/v_j^{1/2}$ vs. $v_j^{1/2}$. Applying this methodology, capacitive and diffusion-controlled contributions to energy storage were calculated over the entire CVs using ΔV = 0.2 V voltage steps. First, it is confirmed that, indeed, at the start of regime II (cycle 3), energy storage processes have contributions from faradaic (battery) processes and capacitive processes. Discharge times in a GCPL experiment and sweeping time using CV were calculated and determined to be similar for experiments at the following equivalent parameters: 0.1 mV s^{-1} and 0.09 A g^{-1}, 0.5 mV s^{-1} and 0.5 A g^{-1} and 1.0 mV s^{-1} and 1.0 A g^{-1}. Therefore, the results obtained from both techniques can be compared. At low rates (0.1 mV s^{-1}, comparable to the GCPL study at 0.05 A g^{-1}), the capacitive contribution was 52.8% (Fig. 9d). The capacitive contributions to energy storage increased as the scanning rate increased. For instance, it was 76.4% for a scan rate of 1.0 mV s^{-1} (comparable to the GCPL study at 1.0 A g^{-1}). A graphical illustration of the contribution of such energy storage processes at 1.0 mV s^{-1} is given in Fig. 9(c). According to the GCPL studies, further cycling at, e.g., 1.0 A g^{-1}, evolved towards capacitive processes (regime III), which is most likely the case, as the capacitive contribution at cycle 3 was already very high (76.4%).

3.8. Discussion

EIS studies point towards very different activation mechanisms undergone at slow (0.05 A g^{-1}) and high (1.0 A g^{-1}) cycling current rates. At slow current rates a single activation mechanism takes place leading to an increase of capacity during the first cycling. However, upon further cycling structural transformations led to a compact electrode with a poor electrolyte infiltration, which derived in a capacity decay. In contrast, a high cycling rate induced two activation processes. The first activation process led to a capacity increase followed by a capacity fall. Structural transformations during this capacity fall stage, generating the ball-like structures and porosity (Fig. 7c and d), were the crucial event, induced only at high rates, leading to the second activation process and to the eventual emergence of an electrode of increasing capacity.

Energy storage mechanisms at high cycling rates can be summarized as follows:

Regime I (battery processes dominate). At cycles 1 to 2, the capacity fell as per SEI and “polymeric-like” film formation. CE increased as per the evolution from irreversible processes at cycle 1 to a comparatively more reversible regime from cycle 2 and following.

Regime II (battery and pseudocapacitive processes dominate). This regime comprises 2 stages:

Capacity rise 1, activation 1. Here activation process 1 takes place, consisting of opening of meso-/microporosity and SEI thinning/breaking. Energy storage processes are fairly reversible.

Capacity fall-initial stage. Cycling induced major electrode structural changes that lead to bulk electrolyte infiltration in a microsized structure consisting of ball-like structures and microsized pores. The SEI was destroyed in this structure. The formation of microsized ball-like structures and a poorer charge transfer inside them lead to a decreasing capacity. A slowly decreasing of CE described a small irreversibility, indicating the evolution from battery/pseudocapacitive to only pseudocapacitive processes.

Regime III (pseudocapacitive and double layer capacitive process dominate). This regime comprises 2 stages:

Capacity fall-final stage and equilibrium. Here, the same electrode structure as in the previous stage prevailed but evolved to larger ball-like structures and smaller pores merging together into a continuum. This marked the end of the capacity fall leading to an equilibrium stage, which took place through several decades of cycles, and where no major structural and physical changes occurred.

Capacity rise 2, activation 2. This stage was started by a major structural event, activation 2, where the merged ball-like structures collapsed into smaller vertically aligned nanostructures giving place to a totally newly structured electrode with a high surface area, well infiltrated with electrolyte and forming a new SEI. Further cycling improved electrolyte infiltration and enhanced surface area available for storage, resulting in an increasing storage consisting of capacitive processes. As expected from capacitive processes, storage in this electrode was highly reversible.

3.9. Rate performance

The rate performance of 2D MoS_2 electrodes was studied. The 2D MoS_2 electrode showed a superior rate performance as com-

pared to the raw MoS_2 electrode in a current range of 0.05 to 2.0 A g^{-1} (Fig. 10a).

Then, the rate performance of the activated 2D MoS_2 electrodes (after long-term cycling at high-rates) was investigated. First, the capacities of the precycled electrodes (Fig. 10b and c) were lower than in the fresh electrode (Fig. 10a). For instance, for the precycled electrode at 0.5 A g^{-1}, the discharge capacity at 0.05 A g^{-1} was 698 mA h g^{-1} (cycle 502) (Fig. 10b), which is 81% of the capacity of a fresh electrode (851.4 mA h g^{-1} at cycle 2) (Fig. 10a). This is expected after precycling, which rendered a totally restructured electrode that stored charge mainly by capacitive processes. Although, at the precycling stage, the electrode followed a continuously raising capacity trend, it did not reach the initial values at the first decade of the cycling test (Fig. 6a).

Second, remarkably, the capacities of a precycled electrode (Fig. 10b and c) were more stable than a fresh electrode (Fig. 10a). Moreover, the capacities at most scan rates followed a similar trend than for the long-term cycling (Fig. 6a and b), i.e., a fall-rise trend followed by a steady trend. e.g., at 0.5, 1.0 and 2.0 A g^{-1} (Fig. 10b,c).

Third, the capacity recovery for the electrode precycled at 1.0 A g^{-1} for 1000 cycles (Fig. 10c) was poorer as compared to the one precycled at 0.5 A g^{-1} (Fig. 10b), e.g., capacities obtained at current rates > 1.0 A g^{-1}, indicating that the rate performance of the activated 2D MoS_2 electrode is related to the precycling rates.

At the end of the rate test, the structural morphology of the activated 2D MoS_2 electrodes was evaluated by ex-situ SEM. Flower-like nanostructures were observed for both electrodes (Fig. S12). A uniform morphology and absence of cracks, demonstrated that the reactivated electrodes exhibited a remarkable structural stability.

It is worth noticing that the 2D MoS_2 electrodes here presented are free of conductive additives. Most reports to date enhance the capacity by combining MoS_2 with a form of carbon, i.e., graphene or carbon nanofibers (Table S1). Unfortunately, those electrodes still suffer from cycling stability and reports are limited to < 500 cycles. The precycled 2D MoS_2 electrodes showed a slightly lower capacity than previous reports but with an improved cycling stability up to 1410 cycles, with the additional advantage of precluding the dead weight of binders, which undermines energy density. The rate performance of our 2D MoS_2 electrodes is comparable to those of MoS_2/carbon electrodes, e.g., MoS_2@CNF, 3D-NCNT@MoS_2, and MoS_2@carbon (Table S2). Future work involving heterostructuring of 2D MoS_2 with other 2D nanomaterials should bring a further improvement of capacity, cyclability and rate performance.

4. Conclusions

2D MoS_2 electrodes were manufactured using scalable LPE and spray deposition methods. The energy storage processes of 2D MoS_2 electrodes were investigated. Electrochemical methods and Raman studies revealed reversible conversion processes. Nevertheless, SEI formation, accompanied by another polymeric-like film formation, contributed to irreversible processes during the first cycles. Then, an intriguing phenomenon of rise of capacity over cycling at high rates was investigated. A range of electrochemical and microscopy studies revealed the details of underlying physical activation mechanisms induced by high-rate cycling. Induced profound electrode structural changes resulted in an evolution of physical and electrochemical properties such as reaction kinetics, and SEI resistance. At the final stage, the activation process delivered a capacitive electrode of a continuously raising capacity. Activated electrodes were capable of delivering up to 81% of the capacity of a pristine electrode and showed superior cycling stability than previously reported MoS_2-based electrodes, which, unlike this work, incorporate binders and conductive additives.

Activation mechanisms proved to be a suitable methodology to enhance the cycling stability of 2D MoS_2 electrodes via induced capacitive processes. Future work should focus on fine tuning the precycling current rates to obtain an optimized balance between capacity and cycling stability.

More importantly, the use of 2D nanomaterials and activation mechanisms, here devised, can be a strategy to overcome similar performance problems of other intercalation/conversion materials. This work paves the way for future development of high performance electrodes based in 2D nanomaterials where energy density could be improved by the suitable combination of different chemistries.

Declaration of competing interest

The authors declare that they have no known competing financial interests or personal relationships that could have appeared to influence the work reported in this paper.

Acknowledgments

TL acknowledges the financial support from the China Scholarship Council (CSC grant. 201808330389). BMS acknowledges the Helmholtz Association for a Helmholtz ERC Recognition Award (ERC-RA-0028).

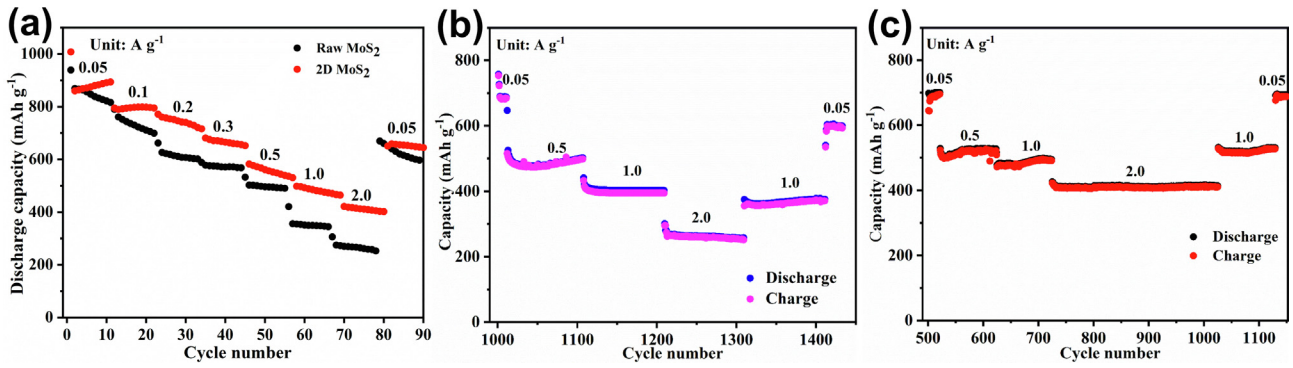

Fig. 10. (a) Rate performance curves of 2D MoS_2 and raw MoS_2 electrodes measured at a range of 0.05 to 2.0 A g^{-1} current rates. (b,c) Rate performance evaluation of 2D MoS_2 electrodes after long-term cycling tests: (b) Capacity vs cycles curves at various current rates after a 500 cycles test at 0.5 A g^{-1}, (c) Capacity vs cycles curves at various rates after a 1000 cycles test at 1.0 A g^{-1}.

The TEM characterisation experiments were performed at the Karlsruhe Nano Micro Facility (KNMF), a Helmholtz research infrastructure operated at KIT. This work contributes to the research performed at the Centre for Electrochemical Energy Storage Ulm-Karlsruhe (CELEST).

Appendix A. Supplementary material

UV-Vis Spectra; SEM images of raw MoS_2 powder; XRD patterns of the cellulose acetate film and 2D MoS_2; further details of Rietveld refinement; further Raman data; electrochemical characterisation of raw MoS_2 electrodes; SEM images of raw pristine MoS_2 electrodes; SSA and pore size data of raw and 2D MoS_2; GCPL at high rates of raw MoS_2 electrodes; SEM images of raw MoS_2 electrodes after GCPL tests at high current rates; energy storage processes of raw MoS_2 electrodes; further EIS of 2D MoS_2 electrodes; SEM images of precycled electrodes; a performance comparison table; XPS data. Supplementary data to this article can be found online at https://doi.org/10.1016/j.jechem.2022.11.007.

References

[1] Y.E. Durmus, H. Zhang, F. Baakes, G. Desmaizieres, H. Hayun, L. Yang, M. Kolek, V. Küpers, J. Janek, D. Mandler, S. Passerini, Y. Ein-Eli, Adv. Ener. Mater. 10 (2020) 2000089.
[2] M. Armand, J.M. Tarascon, Nature 451 (2008) 652–657.
[3] J. Figgener, P. Stenzel, K.-P. Kairies, J. Linßen, D. Haberschusz, O. Wessels, G. Angenendt, M. Robinius, D. Stolten, D.U. Sauer, J. Energy Storage 29 (2020).
[4] S. Goriparti, E. Miele, F. De Angelis, E. Di Fabrizio, R. Proietti Zaccaria, C. Capiglia, J. Power Sources 257 (2014) 421–443.
[5] R. Kotz, M. Carlen, Electrochim. Acta 45 (2000) 2483–2498.
[6] N.S. Choi, Z. Chen, S.A. Freunberger, X. Ji, Y.K. Sun, K. Amine, G. Yushin, L.F. Nazar, J. Cho, P.G. Bruce, Angew. Chem. Int. Ed. 51 (2012) 9994–10024.
[7] T. Stephenson, Z. Li, B. Olsen, D. Mitlin, Energy Environ. Sci. 7 (2014) 209–231.
[8] S.Z. Butler, S.M. Hollen, L. Cao, Y. Cui, J.A. Gupta, H.R. Gutiérrez, T.F. Heinz, S.S. Hong, J. Huang, A.F. Ismach, E. Johnston-Halperin, M. Kuno, V.V. Plashnitsa, R.D. Robinson, R.S. Ruoff, S. Salahuddin, J. Shan, L. Shi, M.G. Spencer, M. Terrones, W. Windl, J.E. Goldberger, ACS Nano 7 (2013) 2898–2926.
[9] M. Chhowalla, H.S. Shin, G. Eda, L.-J. Li, K.P. Loh, H. Zhang, Nat. Chem. 5 (2013) 263–275.
[10] X. Huang, Z. Zeng, H. Zhang, Chem. Soc. Rev. 42 (2013) 1934–1946.
[11] V. Nicolosi, M. Chhowalla, M.G. Kanatzidis, M.S. Strano, J.N. Coleman, Science 340 (2013) 1226419-1226419.
[12] B. Mendoza-Sánchez, Y. Gogotsi, Adv. Mater. 28 (2016) 6104–6135.
[13] X. Zhao, B. Mendoza-Sanchez, P.J. Dobson, P.S. Grant, Nanoscale 3 (2011) 839–855.
[14] B. Mendoza-Sánchez, B. Rasche, V. Nicolosi, P.S. Grant, Carbon 52 (2013) 337–346.
[15] J. Coelho, B. Mendoza-Sánchez, H. Pettersson, A. Pokle, E.K. McGuire, E. Long, L. McKeon, A.P. Bell, V. Nicolosi, 2D Materials 2 (2015). 025005.
[16] B. Mendoza-Sánchez, J. Coelho, A. Pokle, V. Nicolosi, Electrochim. Acta 174 (2015) 696–705.
[17] B. Mendoza-Sánchez, J. Coelho, A. Pokle, V. Nicolosi, Electrochim. Acta 192 (2016) 1–7.
[18] Y. Qiu, Y. Chen, J. Phy. Chem. C 119 (2015) 23813–23819.
[19] C. Backes, T.M. Higgins, A. Kelly, C. Boland, A. Harvey, D. Hanlon, J.N. Coleman, Chem. Mater. 29 (2016) 243–255.
[20] J.N. Coleman, M. Lotya, A. O'Neill, S.D. Bergin, P.J. King, U. Khan, K. Young, A. Gaucher, S. De, R.J. Smith, I.V. Shvets, S.K. Arora, G. Stanton, H.Y. Kim, K. Lee, G. T. Kim, G.S. Duesberg, T. Hallam, J.J. Boland, J.J. Wang, J.F. Donegan, J.C. Grunlan, G. Moriarty, A. Shmeliov, R.J. Nicholls, J.M. Perkins, E.M. Grieveson, K. Theuwissen, D.W. McComb, P.D. Nellist, V. Nicolosi, Science 331 (2011) 568–571.
[21] A. O'Neill, U. Khan, J.N. Coleman, Chem. Mater. 24 (2012) 2414–2421.
[22] G.S. Bang, K.W. Nam, J.Y. Kim, J. Shin, J.W. Choi, S.Y. Choi, ACS Appl. Mater. Inter. 6 (2014) 7084–7089.
[23] J. Rodriguez-Carvajal, Abstracts of the Satellite Meeting on Powder Diffraction of the XV Congress of the IUCr, IUCr, Toulouse, 1990, p. 127.
[24] H.N. He, D. Sun, Y.G. Tang, H.Y. Wang, M.H. Shao, Energy Storage Mater. 23 (2019) 233–251.
[25] H. Li, Q. Zhang, C.C.R. Yap, B.K. Tay, T.H.T. Edwin, A. Olivier, D. Baillargeat, Adv. Funct. Mater. 22 (2012) 1385–1390.
[26] J. Rodriguez-Carvajal, An Introduction to The Program Fullprof, Scientific Research Publishing Inc., Irvine, 2001, pp. 58,103-104,117-118.
[27] J.-F. Bérar, P. Lelann, J. Appl. Crystallogr. 24 (1991) 1–5.
[28] K.S. Liang, R.R. Chianelli, F.Z. Chien, S.C. Moss, J. Non-Crystal, Solids 79 (1986) 251–273.
[29] M.P. De la Rosa, S. Texier, G. Berhault, A. Camacho, M.J. Yácaman, A. Mehta, S. Fuentes, J.A. Montoya, F. Murrieta, R.R. Chianelli, J. Cata. 225 (2004) 288–299.
[30] L. Wang, Z. Xu, W. Wang, X. Bai, J. Am. Chem. Soc. 136 (2014) 6693–6697.
[31] Z. Zhu, Y. Tang, W.R. Leow, H. Xia, Z. Lv, J. Wei, X. Ge, S. Cao, Y. Zhang, W. Zhang, H. Zhang, S. Xi, Y. Du, X. Chen, Angew. Chem. Int. Ed. 58 (2019) 3521–3526.
[32] Y. Wang, Z. Ma, Y. Chen, M. Zou, M. Yousaf, Y. Yang, L. Yang, A. Cao, R.P. Han, Adv. Mater. 28 (2016) 10175–10181.
[33] J. Xiao, D. Choi, L. Cosimbescu, P. Koech, J. Liu, J.P. Lemmon, Chem. Mater. 22 (2010) 4522–4524.
[34] S. Chen, L. Wang, R. Shao, J. Zou, R. Cai, J. Lin, C. Zhu, J. Zhang, F. Xu, J. Cao, J. Feng, J. Qi, P. Gao, Nano Energy 48 (2018) 560–568.
[35] Z. Li, A. Ottmann, Q. Sun, A.K. Kast, K. Wang, T. Zhang, H.-P. Meyer, C. Backes, C. Kübel, R.R. Schröder, J. Xiang, Y. Vaynzof, R. Klingeler, J. Mater. Chem. A 7 (2019) 7553–7564.
[36] L. Zhang, D. Sun, J. Kang, J. Feng, H.A. Bechtel, L.W. Wang, E.J. Cairns, J. Guo, Nano Lett. 18 (2018) 1466–1475.
[37] T. Livneh, J.E. Spanier, 2D Materials 2 (2015) 035003.
[38] C. Lee, H. Yan, L.E. Brus, T.F. Heinz, J. Hone, S. Ryu, ACS Nano 4 (2010) 2695–2700.
[39] G.L. Frey, R. Tenne, M.J. Matthews, M.S. Dresselhaus, G. Dresselhaus, Phy. Rev. B 60 (1999) 2883–2892.
[40] S. Jimenez Sandoval, D. Yang, R.F. Frindt, J.C. Irwin, Phys. Rev. B Condens. Matter. 44 (1991) 3955–3962.
[41] M. Calandra, Phy. Rev. B 88 (2013).
[42] D. Yang, S.J. Sandoval, W.M.R. Divigalpitiya, J.C. Irwin, R.F. Frindt, Phy. Rev. B 43 (1991) 12053–12056.
[43] G. Du, Z. Guo, S. Wang, R. Zeng, Z. Chen, H. Liu, Chem. Commun. 46 (2010) 1106–1108.
[44] S.J. An, J. Li, C. Daniel, D. Mohanty, S. Nagpure, D.L. Wood, Carbon 105 (2016) 52–76.
[45] S. Laruelle, S. Grugeon, P. Poizot, M. Dolle, L. Dupont, J.M. Tarascon, J. Electrochem. Soc. 149 (2002) A627–A634.
[46] C. Chen, N. Ding, L. Wang, Y. Yu, I. Lieberwirth, J. Power Sources 189 (2009) 552–556.
[47] C. Yang, J. Feng, F. Lv, J. Zhou, C. Lin, K. Wang, Y. Zhang, Y. Yang, W. Wang, J. Li, S. Guo, Adv. Mater. 30 (2018) e1800036.
[48] J.S. Edge, S. O'Kane, R. Prosser, N.D. Kirkaldy, A.N. Patel, A. Hales, A. Ghosh, W. Ai, J. Chen, J. Yang, S. Li, M.-C. Pang, L. Bravo Diaz, A. Tomaszewska, M.W. Marzook, K.N. Radhakrishnan, H. Wang, Y. Patel, B. Wu, G.J. Offer, Phy. Chem. Chem. Phy. 23 (2021) 8200-8221.
[49] X. Liu, X. Zhu, D. Pan, R. Soc, Open. Sci. 5 (2018).
[50] C. Choi, D.S. Ashby, D.M. Butts, R.H. DeBlock, Q. Wei, J. Lau, B. Dunn, Nat. Rev. Mater. 5 (2019) 5–19.
[51] V. Augustyn, P. Simon, B. Dunn, Energy Environ. Sci. 7 (2014) 1597–1614.
[52] W. Choi, H.-C. Shin, J.M. Kim, J.-Y. Choi, W.-S. Yoon, J. Electrochem. Sci. Technol. 11 (2020) 1–13.
[53] Y. Zheng, H.J. Seifert, H. Shi, Y. Zhang, C. Kübel, W. Pfleging, Electrochim. Acta 317 (2019) 502–508.
[54] J. Bisquert, G. Garcia-Belmonte, P. Bueno, E. Longo, L.O.S. BulhÃµes, J. Electroanal. Chem. 452 (1998) 229–234.
[55] G.J. Brug, A.L.G. van den Eeden, M. Sluyters-Rehbach, J.H. Sluyters, J. Electroanal. Chem. Interfacial Electrochem. 176 (1984) 275–295.
[56] C. Ho, I.D. Raistrick, R.A. Huggins, J. Electrochem. Soc. 127 (1980) 343–350.
[57] Q. Zhang, J. Pei, G. Chen, C. Bie, J. Sun, J. Liu, Adv. Mater. Inter. 4 (2017) 1700054.
[58] B. Cao, Z. Liu, C. Xu, J. Huang, H. Fang, Y. Chen, J. Power Sources 414 (2019) 233–241.
[59] G.A. Muller, J.B. Cook, H.S. Kim, S.H. Tolbert, B. Dunn, Nano Lett. 15 (2015) 1911–1917.
[60] Y. Fang, X.Y. Yu, X.W.D. Lou, Adv. Mater. 30 (2018) e1706668.